STATE OF THE CLIMATE IN 2019

ANTARCTICA AND THE SOUTHERN OCEAN

T. Scambos and S. Stammerjohn, Eds.

Special Online Supplement to the *Bulletin of the American Meteorological Society,* Vol.101, No. 8, August, 2020

https://doi.org/doi:10.1175/BAMS-D-20-0090.1

Corresponding author: Ted Scambos / tascambos@colorado.edu

STATE OF THE CLIMATE IN 2019

Antarctica and the Southern Ocean

Editors

Jessica Blunden
Derek S. Arndt

Chapter Editors

Peter Bissolli
Howard J. Diamond
Matthew L. Druckenmiller
Robert J. H. Dunn
Catherine Ganter
Nadine Gobron
Rick Lumpkin
Jacqueline A. Richter-Menge
Tim Li
Ademe Mekonnen
Ahira Sánchez-Lugo
Ted A. Scambos
Carl J. Schreck III
Sharon Stammerjohn
Diane M. Stanitski
Kate M. Willett

Technical Editor

Andrea Andersen

BAMS Special Editor for Climate

Richard Rosen

American Meteorological Society

Cover credit:
Adélie penguin on a floating piece of glacier ice near Jenny Island (a few kilometers from the British Antarctic Survey base at Rothera) west of the Antarctic Peninsula. The photo was taken by Ted Scambos on 31 January 2020.

Antarctica and the Southern Ocean is one chapter from the *State of the Climate in 2019* annual report and is available from https://doi.org/10.1175/BAMS-D-20-0090.1. Compiled by NOAA's National Centers for Environmental Information, *State of the Climate in 2019* is based on contributions from scientists from around the world. It provides a detailed update on global climate indicators, notable weather events, and other data collected by environmental monitoring stations and instruments located on land, water, ice, and in space. The full report is available from https://doi.org/10.1175/2020BAMSStateoftheClimate.1.

How to cite this document:

Citing the complete report:
Blunden, J. and D. S. Arndt, Eds., 2020: State of the Climate in 2019. *Bull. Amer. Meteor. Soc.,* **101** (8), Si–S429, https://doi.org/10.1175/2020BAMSStateoftheClimate.1.

Citing this chapter:
Scambos, T. and S. Stammerjohn, Eds., 2020: Antarctica and the Southern Ocean [in "State of the Climate in 2019"]. *Bull. Amer. Meteor. Soc.,* **101** (8), S287–S320, https://doi.org/10.1175/BAMS-D-20-0090.1.

Citing a section (example):
Reid, P., S. Stammerjohn, R. A. Massom, S. Barreira, T. Scambos, and J. L. Lieser, 2020: Sea ice extent, concentration, and seasonality [in "State of the Climate in 2019"]. *Bull. Amer. Meteor. Soc.,* **101** (8), S304–S306, https://doi.org/10.1175/BAMS-D-20-0090.1.

Editor and Author Affiliations (alphabetical by name)

Abrahamsen, E. Povl, Polar Oceans Group, British Antarctic Survey, Cambridge, United Kingdom
Barreira, Sandra, Argentine Naval Hydrographic Service, Buenos Aires, Argentina
Bitz, Cecilia M., Atmospheric Sciences Department, University of Washington, Seattle, Washington
Butler, Amy, NOAA/ESRL Chemical Sciences Division, Boulder, Colorado
Clem, Kyle R., School of Geography, Environment and Earth Sciences, Victoria University of Wellington, Wellington, New Zealand
Colwell, Steve, British Antarctic Survey, Cambridge, United Kingdom
Coy, Lawrence, Science Systems and Applications, Inc., NASA Goddard Space Flight Center, Greenbelt, Maryland
de Laat, Jos, Royal Netherlands Meteorological Institute (KNMI), DeBilt, Netherlands
du Plessis, Marcel D., Department of Marine Science, University of Gothenburg, Gothenburg, Sweden and Southern Ocean Carbon and Climate Observatory, CSIR, South Africa
Fogt, Ryan L., Department of Geography, Ohio University, Athens, Ohio
Fricker, Helen Amanda, Scripps Institution of Oceanography, University of California-San Diego, San Diego, California
Fyfe, John, Canadian Centre for Climate Modelling and Analysis, University of Victoria, Victoria, British Columbia, Canada
Gardner, Alex S., Jet Propulsion Laboratory, California Insitute of Technology, Pasadena, California
Gille, Sarah T., Scripps Institution of Oceanography, University of California at San Diego, La Jolla, California
Gorte, Tessa, Department of Atmospheric and Oceanic Sciences, University of Colorado-Boulder, Boulder, Colorado
Gregor, L., ETH, Zürich, Switzerland
Hobbs, Will, Australian Antarctic Program Partnership and ARC Centre of Excellence for Climate Extremes (CLEX), University of Tasmania, Hobart, Tasmania, Australia
Johnson, Bryan, NOAA/OAR Earth System Research Laboratory, Global Monitoring Division, and University of Colorado, Boulder, Colorado
Keenan, Eric, Department of Atmospheric and Oceanic Sciences, University of Colorado-Boulder, Boulder, Colorado
Keller, Linda M., Department of Atmospheric and Oceanic Sciences, University of Wisconsin-Madison, Madison, Wisconsin
Kramarova, Natalya A., NASA Goddard Space Flight Center, Greenbelt, Maryland
Lazzara, Matthew A., Department of Physical Sciences, School of Arts and Sciences, Madison Area Technical College, and Space Science and Engineering Center, University of Wisconsin-Madison, Madison, Wisconsin
Lenaerts, Jan T. M., Department of Atmospheric and Oceanic Sciences, University of Colorado-Boulder, Boulder, Colorado
Lieser, Jan L., Bureau of Meteorology, Hobart, Tasmania, Australia, and Institute for Marine and Antarctic Studies, University of Tasmania, Hobart, Tasmania, Australia
Liu, Hongxing, Department of Geography, University of Cincinnati, Cincinnati, Ohio
Long, Craig S., NOAA/NWS National Centers for Environmental Prediction, College Park, Maryland
Maclennan, Michelle, Department of Atmospheric and Oceanic Sciences, University of Colorado-Boulder, Boulder, Colorado
Massom, Robert A., Australian Antarctic Division and Australian Antarctic Program Partnership (AAPP), Hobart, Tasmania, Australia
Massonnet, François, Centre de Recherches sur la Terre et le Climat Georges Lemaître (TECLIM), Earth and Life Institute, Université Catholique de Louvain, Louvain-la-Neuve, Belgium
Mazloff, Matthew R., Scripps Institution of Oceanography, University of California-San Diego, San Diego, California
Mikolajczyk, David, Space Science and Engineering Center, University of Wisconsin-Madison, Madison, Wisconsin
Narayanan, A., Indian Institute of Technology, Madras, Chennai, India
Nash, Eric R., Science Systems and Applications, Inc., NASA Goddard Space Flight Center, Greenbelt, Maryland
Newman, Paul A., NASA Goddard Space Flight Center, Greenbelt, Maryland
Petropavlovskikh, Irina, Cooperative Institute for Research in Environmental Sciences, University of Colorado Boulder, and NOAA/OAR Earth System Research Laboratory, Boulder, Colorado
Pitts, Michael, NASA Langley Research Center, Hampton, Virginia
Queste, Bastien Y., Department of Marine Sciences, University of Gothenburg, Gothenburg, Sweden
Reid, Phillip, Australian Bureau of Meteorology and Australian Antarctic Program Partnership (AAPP), Hobart, Tasmania, Australia
Roquet, F., Department of Marine Sciences, University of Göteborg, Göteborg, Sweden
Santee, Michelle L., NASA Jet Propulsion Laboratory, California Institute of Technology, Pasadena, California
Scambos, Ted A., Earth Science and Observation Center, CIRES, University of Colorado, Boulder Colorado
Stammerjohn, Sharon, Institute of Arctic and Alpine Research, University of Colorado, Boulder, Colorado
Strahan, Susan, Universities Space Research Association, NASA Goddard Space Flight Center, Greenbelt, Maryland
Swart, Sebastiann, Department of Marine Sciences, University of Gothenburg, Gothenburg, Sweden and Department of Oceanography, University of Cape Town, Rondebosch, South Africa
Wang, Lei, Department of Geography and Anthropology, Louisiana State University, Baton Rouge, Louisiana

Editorial and Production Team

Andersen, Andrea, Technical Editor, Innovative Consulting Management Services, LLC, NOAA/NESDIS National Centers for Environmental Information, Asheville, North Carolina
Griffin, Jessicca, Graphics Support, Cooperative Institute for Satellite Earth System Studies, North Carolina State University, Asheville, North Carolina
Hammer, Gregory, Content Team Lead, Communications and Outreach, NOAA/NESDIS National Centers for Environmental Information, Asheville, North Carolina
Love-Brotak, S. Elizabeth, Lead Graphics Production, NOAA/NESDIS National Centers for Environmental Information, Asheville, North Carolina
Misch, Deborah J., Graphics Support, Innovative Consulting Management Services, LLC, NOAA/NESDIS National Centers for Environmental Information, Asheville, North Carolina
Riddle, Deborah B., Graphics Support, NOAA/NESDIS National Centers for Environmental Information, Asheville, North Carolina
Veasey, Sara W., Visual Communications Team Lead, Communications and Outreach, NOAA/NESDIS National Centers for Environmental Information, Asheville, North Carolina

6. Table of Contents

***Please refer to Chapter 8 (Relevant datasets and sources) for a list of all climate variables and datasets used in this chapter for analyses, along with their websites for more information and access to the data.**

6. ANTARCTICA AND THE SOUTHERN OCEAN

T. Scambos and S. Stammerjohn, Eds.

a. Overview—T. Scambos and S. Stammerjohn

Antarctica experienced a dramatic stratospheric warming event in early September 2019 that strongly affected climate patterns in the final four months of the year, and led to the smallest ozone hole since the early 1980s. The event was caused by a series of upward-propagating tropospheric waves in late August, resulting in above-average temperatures in the stratosphere that inhibited polar stratospheric cloud formation and greatly reduced ozone loss. In the troposphere, the Southern Annular Mode (SAM) was strongly negative in the last three months of the calendar year, reflective of anomalously high pressure conditions south of 60°S and weak westerly winds. Together, the stratospheric warming in September and related surface conditions starting thereafter contributed to anomalous warm surface spring conditions, setting several high-temperature records. Meanwhile, anomalously low sea ice extent (below the 1981–2010 mean) persisted throughout 2019, continuing a succession of negative Antarctic sea ice extent anomalies since September 2016. The year 2019 was also characterized by warm surface ocean conditions and large positive net ocean heat flux anomalies (into the ocean) south of 35°S. In contrast, ice sheet surface mass balance was near normal for the year (compared with 1981–2010), though with high monthly variability due to variable precipitation, sublimation, and summer surface melt. However, the ice sheet continued to lose mass in 2019, not due to surface changes but rather ocean–ice sheet interactions, with the highest rates of mass loss occurring in West Antarctica and Wilkes Land, East Antarctica.

The state of Antarctica's climate, weather, ice, ocean, and ozone in 2019 is presented below. Most sections compare the 2019 anomalies with the 1981–2010 climatology wherever there are available data to do so. The ozone section and the sidebar on stratospheric warming compare the 2019 anomaly to the full record (1980–2019) when such data are available to better emphasize how unusual stratospheric conditions were in 2019. We also include a sidebar on ice sheet changes this year that reviews ice sheet and ice shelf trends over the past three decades. In coming years, this sidebar topic will develop into a separate section detailing annual preliminary assessments of Antarctica's ice mass balance. New subsections on ocean heat uptake and ocean CO_2 uptake are included in our Southern Ocean section. Place names for data sites or climate events noted in this chapter are provided in Fig. 6.1.

Fig. 6.1. Map of stations and other regions discussed in the chapter.

b. Atmospheric circulation and surface observations—K. R. Clem, S. Barreira, R. L. Fogt, S. Colwell, L. M. Keller, M. A. Lazzara, and D. Mikolajczyk

The stratospheric warming anomaly in September was the main circulation feature of 2019 (see Sidebar 6.1), resulting in a record weak stratospheric vortex, an earlier-than-normal seasonal breakdown of the stratospheric vortex (section 6g), and many record-setting positive pressure and temperature anomalies in the troposphere and surface layer during October–December. Prior to the stratospheric warming event, the circulation exhibited typical month-to-month and regional variability. June was characterized by record low temperature and pressure anomalies across the continent. For the Antarctic continent as a whole, 2019 was the second-warmest year on record (since 1979), +0.55°C (+2.1 std. dev.) above the 1981–2010 climatology (based on reanalysis described below and as presented in Fig. 6.2b). This surpasses 2018, which is now the third-warmest year on record. The warmest year in the record is 1980. We used the European Centre for Medium-Range Weather Forecast (ECMWF) fifth-generation atmospheric reanalysis (ERA5; Copernicus Climate Change Service [C3S] 2017) to evaluate atmospheric circulation for the year. Figure 6.2 shows the monthly geopotential height (Fig. 6.2a) and temperature (Fig. 6.2b) anomalies averaged over the polar cap (60°–90°S), and the monthly circumpolar zonal wind anomalies (Fig. 6.2c) averaged over 50°–70°S. The anomalies are contoured, with standard deviations relative to the 1981–2010 monthly climatology overlain as color shading. To investigate the surface climate anomalies, the year was split into five periods, with the periods characterized by differing yet

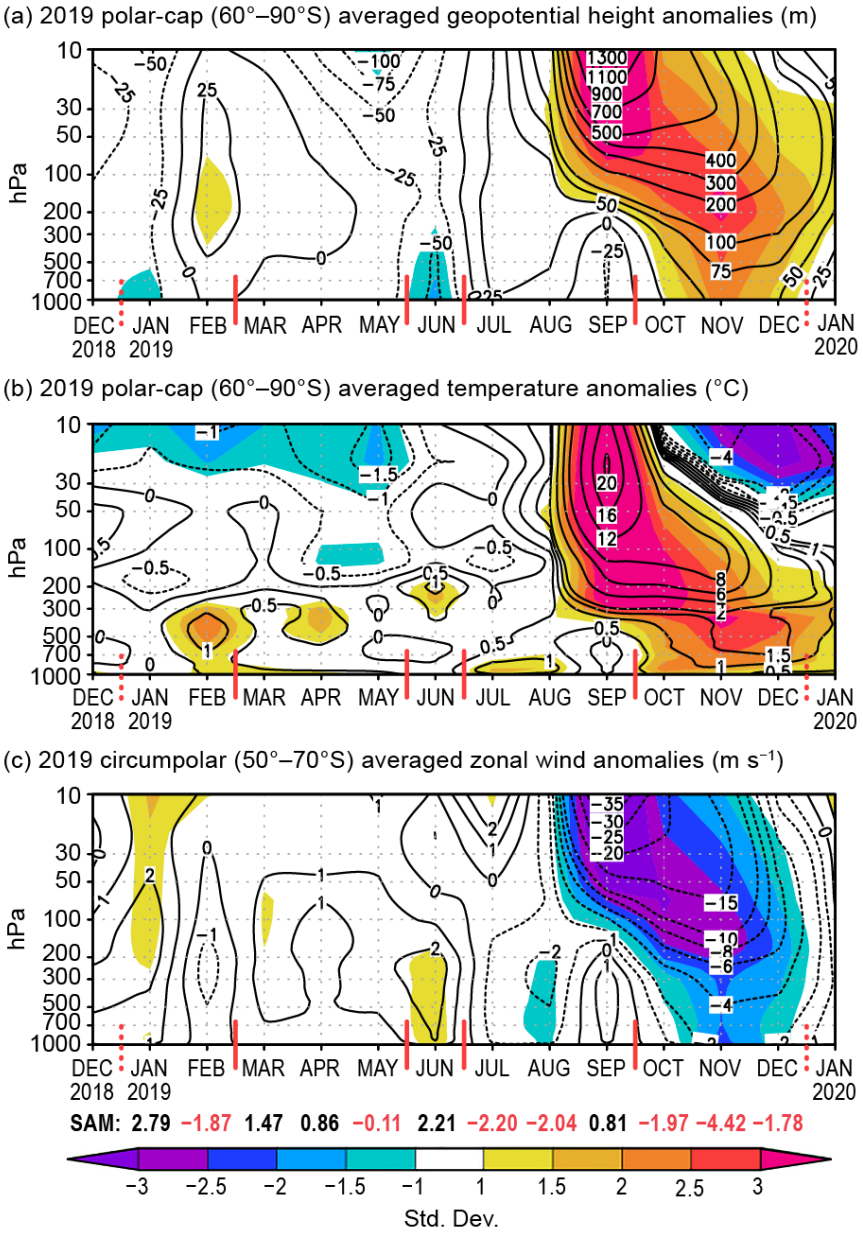

Fig. 6.2. Area-averaged (weighted by cosine of latitude) monthly anomalies over the southern polar region in 2019 relative to 1981–2010. Vertical axes are pressure in hPa. (a) Polar cap (60°–90°S) averaged geopotential height anomalies (contour interval is 25 m up to ±100 m, 100 m from ±100 to ±500 m, and 200 m after ±500 m). (b) Polar cap averaged temperature anomalies (contour interval is 0.5°C up to ±2°C, 2°C between ±2°C and ±8°C, and 4°C after ±8°C). (c) Circumpolar (50°–70°S) averaged zonal wind anomalies (contour interval is 2 m s^{-1} from ±2 m s^{-1} to ±10 m s^{-1} and 5 m s^{-1} after 10 m s^{-1}, with additional contour at ±1 m s^{-1}). Shading depicts std. dev. of monthly anomalies from the 1981–2010 climatological average as indicated by color bar at bottom. (Source: ERA5 reanalysis.) Red vertical bars indicate the five climate periods used in Fig. 6.3; the dashed lines near Dec 2018 and Dec 2019 indicate circulation anomalies wrapping around the calendar year. Values from the Marshall (2003) SAM index are shown below (c) in black (positive values) and red (negative values).

relatively persistent circulation and temperature anomaly patterns: (1) January–February, (2) March–May, (3) June, (4) July–September, and (5) October–December. Standardized surface pressure (contours) and temperature (color shaded) anomalies averaged for each period relative to the 1981–2010 climatology are shown in Fig. 6.3. Monthly temperature and pressure anomalies from select Antarctic staffed (Amundsen–Scott, Marambio, Neumayer, and Syowa) and automated (Gill AWS, Relay Station AWS) weather stations are shown in Fig. 6.4.

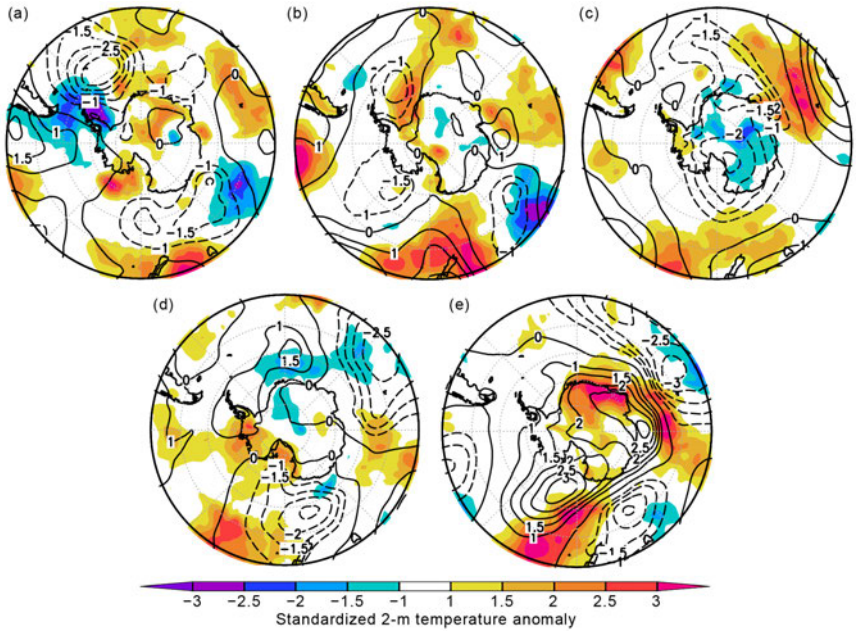

Fig. 6.3. Standardized surface pressure (contours) and 2-m temperature (shaded) anomalies relative to 1981–2010 for (a) Jan–Feb 2019; (b) Mar–May 2019; (c) Jun 2019; (d) Jul–Sep 2019; (e) Oct–Dec 2019. Contour interval is 0.5 std. dev. for surface pressure anomalies with the ±0.5 contour omitted. Shading represents standard deviation of 2-m temperature anomalies. (Source: ERA5 reanalysis.)

The year 2019 began with two centers of anomalous low pressure during January and February (Fig. 6.3a), one located in the southwest South Pacific (–1.5 std. dev.) and one in the South Atlantic (–3 std. dev.). These low-pressure anomalies produced above-average temperatures on the Ross Ice Shelf and the East Antarctic Plateau, but below-average temperatures across the Antarctic Peninsula; the polar cap average mid-tropospheric temperature was +1°C (2 std. dev.) above normal in February (Fig. 6.2b). On the eastern side of the Plateau, Relay Station AWS (Fig. 6.4e) set a record high monthly mean temperature for February (–31.7°C, +6.1°C above normal) and a record high monthly mean wind speed for February (8.2 m s^{-1}, not shown). Monthly mean temperatures on the Antarctic Peninsula (i.e., Marambio Station; Fig. 6.4b) were below normal for January and February, but no records were set.

The austral autumn months (March–May) were relatively quiescent, with pressures and temperatures close to the climatological average across most of the continent (Figs. 6.2, 6.3b). The exception was over the far southern Atlantic Ocean where low-pressure systems were present most of the period, resulting in a deep low-pressure anomaly (–1.5 std. dev.) in the Weddell Sea. This produced above-average temperatures (+2.5 std. dev.) over much of the eastern Weddell Sea, while another low-pressure anomaly (–1.5 std. dev.) over the eastern Ross Sea advected the anomalous warm air from the Weddell Sea across interior West Antarctica and onto the Ross Ice Shelf. The cyclonic conditions in the Weddell Sea dissipated temporarily during March and were replaced by anomalous high pressure over the southern Atlantic Ocean (not shown). During this time, Neumayer Station reported a record low monthly mean temperature of –17°C (–4.2°C below normal) in March (Fig. 6.4c).

During June, the circulation became quite anomalous. Pressures were generally 1.5–2.5 std. dev. below normal, temperatures were 1–2 std. dev. below normal across most of the continent (Fig. 6.3c), and the circumpolar zonal winds in the troposphere were more than 2 m s^{-1} (1 std. dev.) above normal (Fig. 6.2c). The station-based Southern Annular Mode (SAM) index (Marshall 2003), which measures the anomalous pressure gradient between the Southern Hemisphere (SH) middle latitudes and Antarctica, was strongly positive in June, reaching +2.21 (10th highest for June on record since 1957). The Ferrell, Marble Point, and Gill AWSs on the Ross Ice Shelf (Fig. 6.4f) as well as Possession Island AWS in the Ross Sea, all reported record low monthly mean pressures in June that were 13–14.5 hPa below normal. On the Plateau, Dome C II AWS (631.4 hPa, –16.0 hPa below

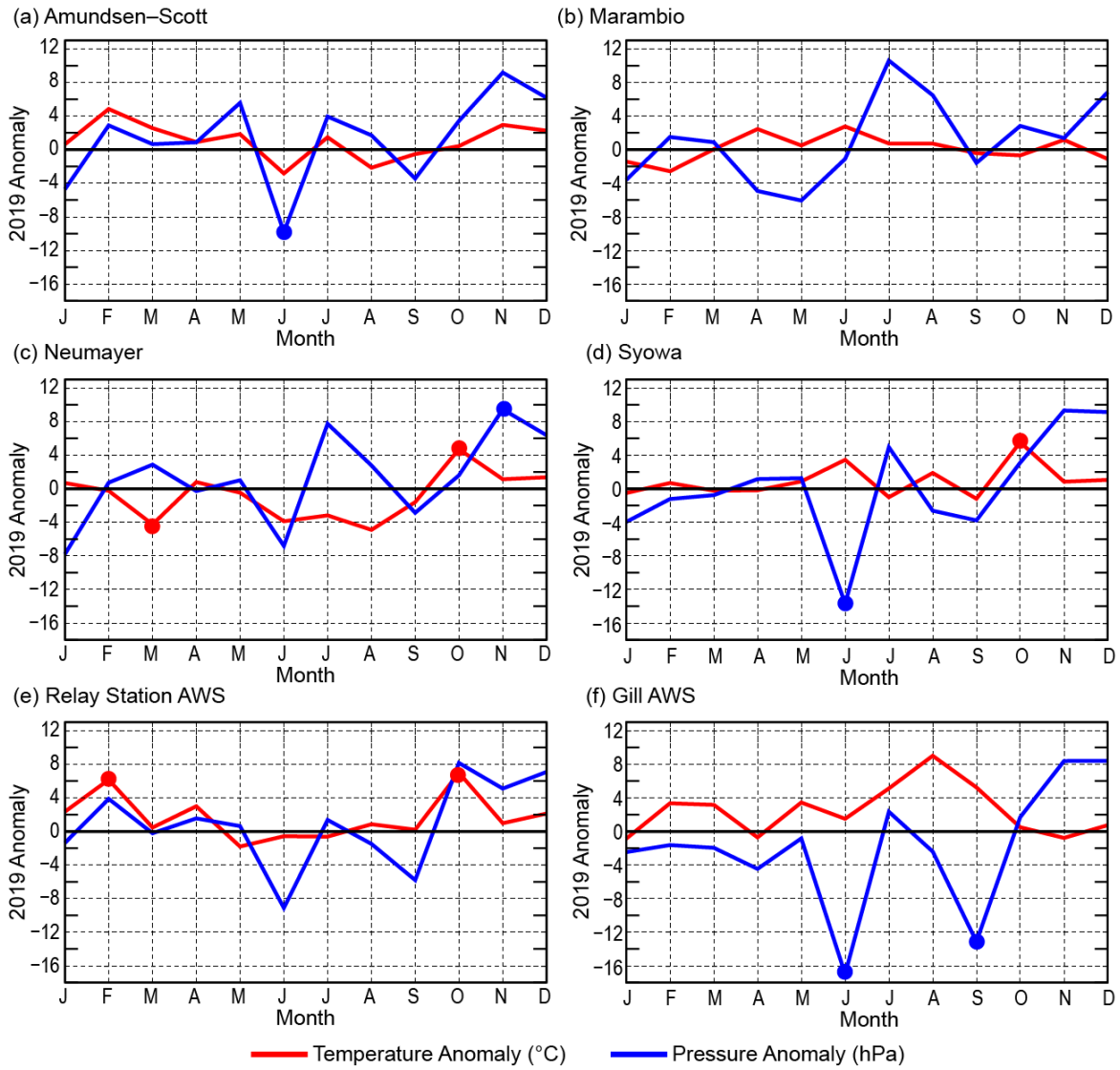

Fig. 6.4. Monthly Antarctic climate anomalies during 2019 at six representative stations (four staffed [a]–[d], and two automatic [e]–[f]). Anomalies for temperature (°C) are shown in red and anomalies for MSLP/surface pressure (hPa) are shown in blue, with filled circles denoting record anomalies for a given month. Anomalies for the four staffed stations are based on differences from the monthly 1981–2010 averages; for AWS, Gill is based on 1985–2014 averages and Relay Station is based on 1995–2010 averages. Observational data used to calculate record values start in 1957 for Amundsen–Scott and Syowa, 1970 for Marambio, 1981 for Neumayer, 1985 for Gill AWS, and 1995 for Relay Station AWS. The surface station data are available online at https://legacy.bas.ac.uk/met/READER/data.html (Turner et al. 2004) and ftp://amrc.ssec.wisc.edu/pub/aws.

normal); Vostok (612.4 hPa, –11.7 hPa); and Amundsen–Scott (671.0 hPa, –9.8 hPa, Fig. 6.4a) all had record low monthly mean pressures in June, as did Syowa Station (973.5 hPa, –13.7 hPa) on the Queen Maud Land coast. Relay Station AWS had very low monthly mean pressure (626.8 hPa, –9.1 hPa), but no record was set. In contrast to the below-average temperatures and pressures over the main Antarctic continent, the Antarctic Peninsula experienced slightly negative pressure anomalies and above-average temperatures in June due to relatively warm west-northwesterly flow from the Bellingshausen Sea.

The overall circulation pattern quickly changed during July–September when it became marked by a weakening of the tropospheric zonal winds (Fig. 6.2c), positive pressure anomalies over the Antarctic Peninsula, and a very strong negative pressure anomaly (–2.5 std. dev.) south of New Zealand that stretched poleward into the Ross Sea. Much of the South Pacific experienced

warm, northerly flow that brought positive temperature anomalies over the Ross Ice Shelf and Marie Byrd Land (Fig. 6.3d). Possession Island AWS observed a record high monthly mean temperature of –11.7°C (+8.6°C above normal) for July. In West Antarctica, Byrd AWS had positive temperature anomalies of +2.9 and +4.9°C during July and August, respectively. In September, strong negative pressure anomalies briefly developed at the surface across most of the continent with a pronounced zonal wave-3 structure (not shown). These pressure anomalies were strongest over the Ross Ice Shelf where Ferrell (971.6 hPa, –9.8 hPa), Gill (965.1 hPa, –9.8 hPa; Fig. 6.4f), and Possession Island (966.6 hPa, –8.3 hPa) AWSs all had record low monthly mean pressures for September. Ferrell also set a record high monthly mean wind speed of 9.5 m s^{-1} in September (not shown).

The most dramatic feature of the 2019 circulation was a record-setting stratospheric warming event that developed during September (Fig. 6.2; see Sidebar 6.1 for more details). Initially confined mainly above 300 hPa and averaged poleward of 60°S, this event was marked by strong positive geopotential height anomalies of up to 1300 m and a positive temperature anomaly of 20°C at the 30–20 hPa level. This was associated with a significant weakening of the stratospheric polar vortex by up to 35 m s^{-1}. All three anomalies in Fig. 6.2 exceeded 3 std. dev. from the climatological mean, and at the 30–10 hPa level, all three anomalies were the largest on record in the ERA5 data beginning in 1979.

The circulation anomalies in the stratosphere progressed downward into the troposphere during October–December (Fig. 6.2). In October, higher-than-normal pressures and temperatures at the surface (Fig. 6.3e) reversed the general trend of the preceding months. The strongest warming (>3 std. dev.) occurred across Queen Maud Land. Neumayer (–13.2°C, +4.7°C; Fig. 6.4c) and Syowa (–8.0°C, +5.5°C; Fig. 6.4d) stations, as well as Relay Station AWS (–42.3°C, +7.0°C; Fig. 6.4e), all set record high temperatures for October, with Neumayer also setting a record high pressure in November (994.2 hPa, +9.5 hPa). There was a very strong anticyclonic (>3 std. dev.) anomaly over the Ross Sea region. Marble Point AWS tied its record high pressure for November (982.8 hPa, +11.0 hPa), while Ferrell, Possession Island, and Gill AWSs (Fig. 6.4f) had near-record high pressure for November (8–11.5 hPa above normal). The SAM index reached its largest negative mean monthly value of the year in November of –4.42 (second lowest for November on record since 1957). In the Antarctic interior, Relay Station AWS, Amundsen–Scott (Fig. 6.4a), and Vostok stations all had higher-than-normal pressure for October through December, but no records were set. In the Weddell Sea region, Halley Station set a record high monthly mean temperature of –3.1°C (+2.1°C) in December.

Sidebar 6.1: **The 2019 southern stratospheric warming**—P. NEWMAN, E. R. NASH, N. KRAMAROVA, A. BUTLER

The Southern Hemisphere (SH) polar stratosphere is typically quite cold in the July–September period with temperatures well below 195 K in the lower stratosphere (~50 hPa). In September 2019, the southern polar stratosphere was disrupted by a sudden warming event. While warmings are typical in the Northern Hemisphere (NH), there has been only one major stratospheric warming observed in the SH historical record, in 2002. Warmings are characterized by a dramatic warm-up of the polar stratosphere, a deceleration of the westerly polar night jet, and an increase of polar ozone. Warmings are driven by planetary-scale waves that propagate from the troposphere into the stratosphere on a time-scale of a few days.

There were a series of wave events that drove the changes seen in September and October 2019. Figure SB6.1a shows the 45°–75°S eddy heat flux (scaled by the square root of the pressure) from 1000 hPa (near surface) to 1 hPa, determined from MERRA-2 reanalysis data (Gelaro et al. 2017). The magnitude of the eddy heat flux is proportional to the vertical component of the wave activity, with upward wave events denoted by negative numbers. Vertical dashed lines are drawn for each of the eddy heat flux events (or minima) observed over the August–November period. There are 10 notable events in this period: 10, 19, 26 August; 4, 15, 30 September; 8, 17, 29 October; 10 November. The peaks of eddy heat flux at 100 hPa then extend, within a few days, up to higher levels (10–1 hPa) as these waves propagate vertically into the middle stratosphere.

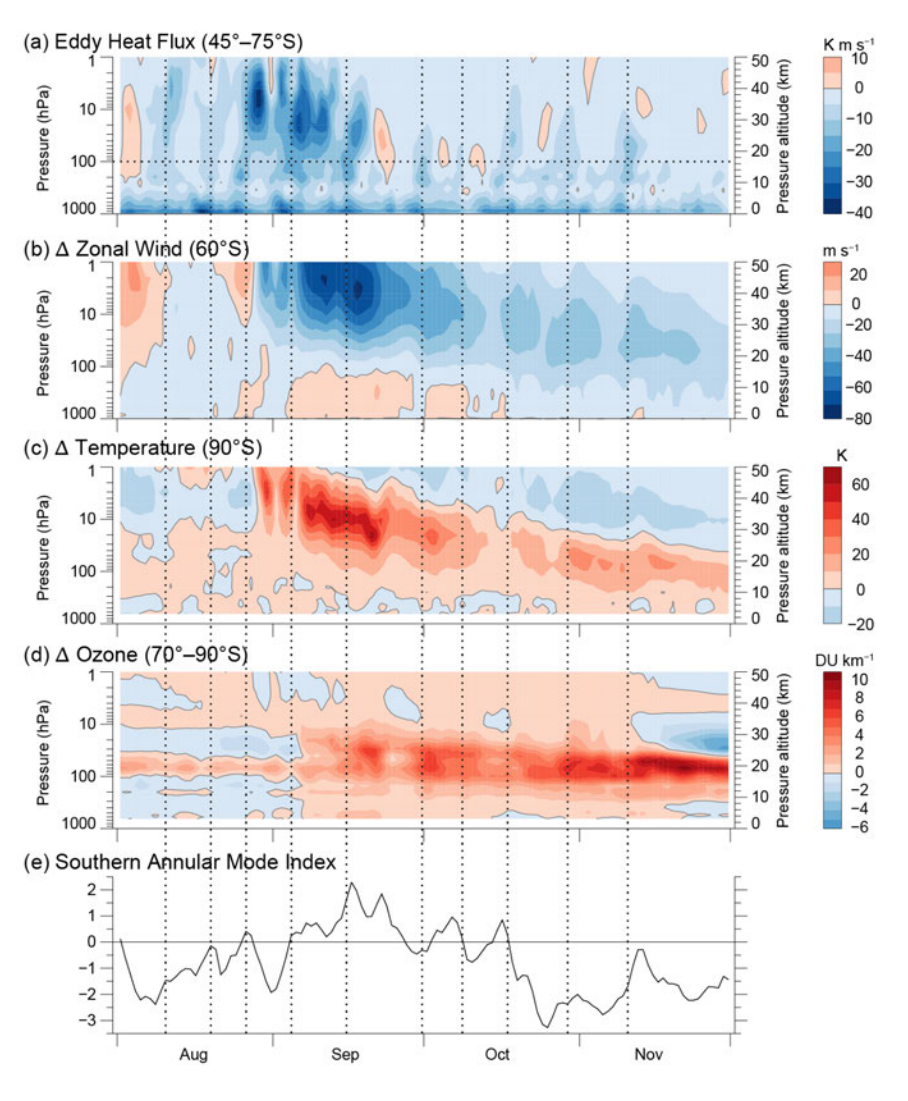

Fig. SB6.1. Daily averaged zonal-mean MERRA-2 quantities for 1 Aug–30 Nov 2019. (a) Eddy heat flux over 45°–75°S (K m^{-1} s^{-1}); departures of: (b) 60°S zonal wind (m s^{-1}); (c) South Pole temperature (K); and (d) polar cap ozone (DU km^{-1}) from the 1980–2018 mean. (e) Daily SAM index (Marshall 2003). Eddy heat flux values (a) are vertically scaled by the square root of pressure. Vertical dashed lines indicate peaks in the strength of the eddy heat flux at 100 hPa, indicated by the horizontal line in (a).

The wave events strongly decelerated the polar night jet by depositing easterly momentum in the middle stratosphere. Figure SB6.1b displays the deviation of the zonal wind at 60°S from a daily 1980–2018 climatology. The wave events led to large decelerations. At 60°S and 10 hPa, the wind decelerated from 87 m s^{-1} on 25 August, to 53 m s^{-1} on 2 September. This was followed by a deceleration to 26 m s^{-1} on 11 September. By 17 September, the zonal wind at 10 hPa had fallen to 11 m s^{-1}. Because the wind did not reverse to easterlies at 10 hPa (a major warming is defined by a reversal of easterly winds at 10 hPa, 60°S), the 2019 August–September warming cannot be categorized as a major warming. However, this large deceleration was unprecedented for this period in the historical record.

The 2019 wave events warmed the polar stratosphere by driving descending motion in the core of the Antarctic polar vortex. Figure SB6.1c displays the deviation of the temperature at 90°S from a daily 1980–2018 climatology, illustrating the warming of the polar stratosphere as a result of the wave events. At the pole, 10-hPa temperature increased from 192 K on 25 August, to 221 K on 2 September, followed by a warming to 267 K on

11 September. The large warming reversed the 90°–50°S thermal gradient as of 6 September and was the earliest reversal in the historical record, even earlier than the September 2002 warming.

The wave events also dramatically increased ozone over the polar region during the key period of ozone depletion in August and September. Figure SB6.1d shows deviations of the ozone density from the 1980–2018 climatology in Dobson Units (DU) per kilometer. The highest ozone density is found in the lower stratosphere (below 10 hPa). Again, large changes of column ozone are associated with the individual wave events, increasing ozone well beyond the 1980–2018 average levels for the dates.

The downward influence of the stratospheric warming on the Southern Annular Mode (SAM; Lim et al. 2018, 2019) did not appear until mid-October (Fig. SB6.1e), when the SAM index went from a positive to a negative value. The SAM variations are in reasonable agreement with Fig. SB6.1b and Fig. 6.2c (below the x-axis), showing how the phase and strength of the annular mode are related to the zonal mean wind in the troposphere. The negative phase of the SAM, which is associated with anomalously hot and dry conditions in eastern Australia (Lim et al. 2019), persisted through at least mid-December and may have contributed to the extreme wildfire and heat conditions observed there during this time.

The series of wave events in August–October 2019 had a profound effect on the SH. The 10 wave events were dominated by a planetary-scale wave-1 pattern and propagated vertically from the troposphere to the stratosphere. These waves decelerated the flow, eroded the polar vortex, warmed the polar region (section 6b), and dramatically increased ozone over Antarctica (section 6h). While this event was not categorized as a major stratospheric sudden warming, it was the largest warming event observed in the August–September record since 1980.

c. Surface mass balance of the ice sheet—J. Lenaerts, E. Keenan, M. Maclennan and T. Gorte

The grounded portion of the Antarctic Ice Sheet (AIS) is characterized by a frigid continental climate. Even in peak summer, atmospheric temperatures on the main continent are low enough to prevent widespread surface melt (section 6d) or liquid precipitation, unlike the Greenland Ice Sheet (section 5e). With few exceptions (e.g., on the northern Antarctic Peninsula), any meltwater that is produced refreezes locally in the firn. Meltwater runoff is a negligible component of ice sheet mass change on the AIS. On the other hand, sublimation is a significant component of AIS surface mass balance (SMB; Lenaerts and Van Den Broeke 2012; Agosta et al. 2019; Mottram et al. 2020), especially in summer and in the windy escarpment zones of the ice sheet, where blowing snow occurs frequently (>50% of the time; Palm et al. 2018). By far the dominant contributor to AIS SMB, with an approximate magnitude of ~2300 Gt yr^{-1} over the grounded AIS, is solid precipitation, i.e., snowfall.

Atmospheric reanalysis products are important tools for analyzing AIS SMB and its two dominant components, snowfall and sublimation, in near-real time. Here we use the MERRA-2 at 0.5° × 0.625° horizontal resolution (Gelaro et al. 2017) and ERA-5 (ERA-Interim's successor, employing 0.25° horizontal resolution; Copernicus Climate Change Service [C3S] 2017) reanalysis data to analyze the 2019 AIS SMB, its spatial and seasonal characteristics, and also to compare it to the climatological record (1981–2010). Based on recent work comparing reanalysis products with in situ observations on Antarctica, MERRA-2 and ERA-5 stood out as best-performing (Wang et al. 2016; Gossart et al. 2019; Medley and Thomas 2019); however, important biases remain, which are associated with the relatively low resolution of the reanalysis products and poor/no representation of important SMB processes (e.g., blowing snow, clear-sky precipitation).

Acknowledging these limitations, we use these two reanalysis products to provide a time series of (grounded) AIS SMB from 1980 to 2019 (Fig. 6.5a). The 1981–2010 mean SMB is 2159 ± 131 Gt yr^{-1} in MERRA-2 and 2070 Gt yr^{-1} ± 113 Gt yr^{-1} in ERA-5. While both time series show comparable interannual variations, with year-to-year SMB differences of >300 Gt yr^{-1} between dry and wet years, neither of the reanalyses suggest a significant long-term trend in SMB (not shown). Further, although there is apparent better agreement in some periods relative to others, there is no significant trend in the difference between MERRA-2 and ERA-5 over the entire 1980–2019 period ($p = 0.62$).

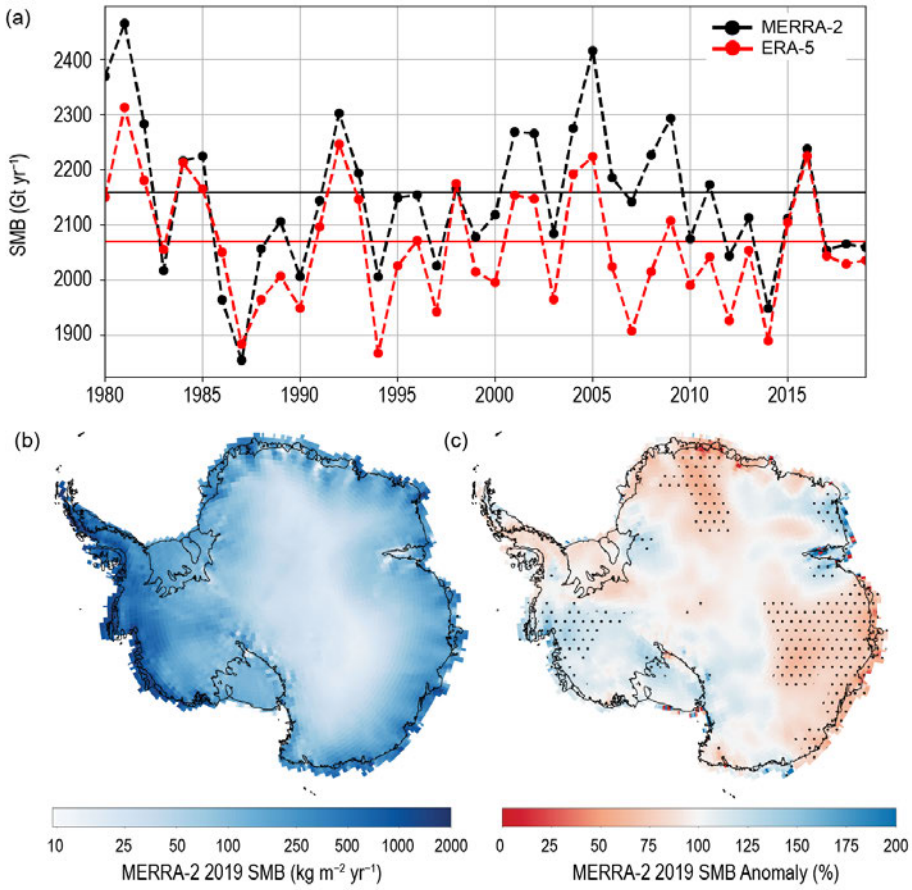

Fig. 6.5. Antarctic surface mass balance (SMB) in 2019. (a) Time series of annual (grounded) Antarctic Ice Sheet (AIS) integrated SMB (in Gt yr^{-1}) from 1980 to 2019, according to MERRA-2 (black) and ERA-5 (in red); horizontal lines are 1981–2010 means, respectively. (b) and (c) 2019 SMB and SMB anomaly relative to 1981–2010 according to MERRA-2. In (c), 2019 SMB anomaly is higher than the 1981–2010 std. dev. in the stippled areas.

The 2019 SMB total and SMB anomaly were 2060 Gt and −99 Gt, respectively, for MERRA-2, and 2036 Gt and −34 Gt, respectively, for ERA-5, thus showing near-normal conditions for 2019 (compared with the 1981–2010 climatology). Because both reanalysis datasets produce similar results, we use MERRA-2 hereafter to focus on spatial and seasonal characteristics of the 2019 SMB. As described by various studies, AIS SMB is typically relatively high (>500 mm w.e.) in the coastal areas of the ice sheet and decreases sharply from the coast upward and poleward on the ice sheet; the same was true for 2019 (Fig. 6.5b) with SMB values being <50 mm w.e. in the high-elevation interior of the East Antarctic Ice Sheet (EAIS). According to MERRA-2, both snowfall and sublimation in 2019 were close to the AIS 1981–2010 mean.

While the 2019 AIS SMB was close to average, the MERRA-2 results indicate substantial regional variability in the 2019 snowfall relative to the mean (Fig. 6.5c). While some AIS regions were characterized by relatively dry conditions, the 2019 SMB was relatively high in other regions. In particular, 2019 SMB was substantially higher than climatology (>125%) in the Amundsen and Bellingshausen glacial basins, thus offsetting part of the dynamic mass loss that is ongoing in that area (Sidebar 6.2). On the other hand, 2019 SMB was exceptionally low compared with the climatology (<75%) in western Queen Maud Land and Wilkes Land, marking a reversal (for this year) of recent high-accumulation trends there (Lenaerts et al. 2013).

Throughout the year, the climatological AIS SMB varies considerably (Fig. 6.6), with a minimum in austral summer (120–140 Gt month^{-1}) and maximum in austral autumn and winter (200–220 Gt month^{-1}). In 2019, this seasonal cycle was amplified, with January–May and September–December being drier than average, while the 2019 winter months (June–August) were characterized by greater-than-average snowfall. Comparing the 2019 anomaly with the long-term mean and standard deviation (black line and gray shading, Fig. 6.6) indicates that the low SMB values in January, May, and December were significant (>1 std. dev.), while

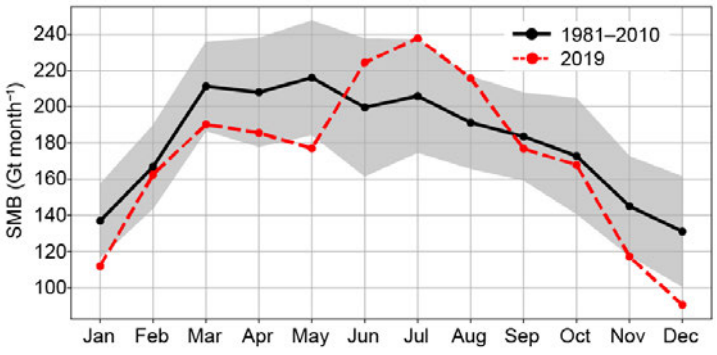

Fig. 6.6. Seasonal cycle of (grounded) Antarctic Ice Sheet (AIS) integrated surface mass balance (SMB) according to MERRA-2 for 2019 (red) and 1981–2010 (black line = mean, gray shading: std. dev.).

July 2019 had substantially more snowfall than climatology. The December dry anomaly, which was preceded by a dry November (~60 Gt cumulative snowfall deficit), may have contributed to early indications of an anomalously high surface melt year for 2019–20 (as mentioned in section 6d and consistent with section 6b). It appears that low snowfall reduced the amount of highly reflective fresh snow on the surface, which lowered the albedo and enhanced the melt–albedo feedback effect early in the 2019/20 melt season.

d. Seasonal melt extent and duration for the ice sheet—L. Wang and H. Liu

Surface melt of the Antarctic Ice Sheet (AIS) is largely confined to the coastal region where it can contribute to surface mass balance (SMB) changes (section 6c). Here, we report on the austral spring–summer 2018/19 melt season; therefore, this analysis does not include the extensive melting that occurred later in 2019 in response to widespread warming (section 6b, Figs. 6.2b, 6.3e). Since Antarctica's melt season extends well into the first few months of the calendar year, a complete assessment of the more recent austral melt season (2019/20) is not yet available but will be highlighted in next year's annual report.

Surface melt of the AIS can be mapped using satellite passive microwave data obtained from the Defense Meteorological Satellite Program (DMSP; Zwally and Fiegles 1994). A nearly continuous record of surface melt exists for the period 1978–present from the DMSP satellite series and earlier Nimbus series satellites. Daily passive microwave brightness temperature observations, using the 19 GHz channel at horizontal polarization acquired by the Special Sensor Microwave–Imager Sounder (SSMIS) onboard the DMSP F17 satellite (ascending passes only), were used to

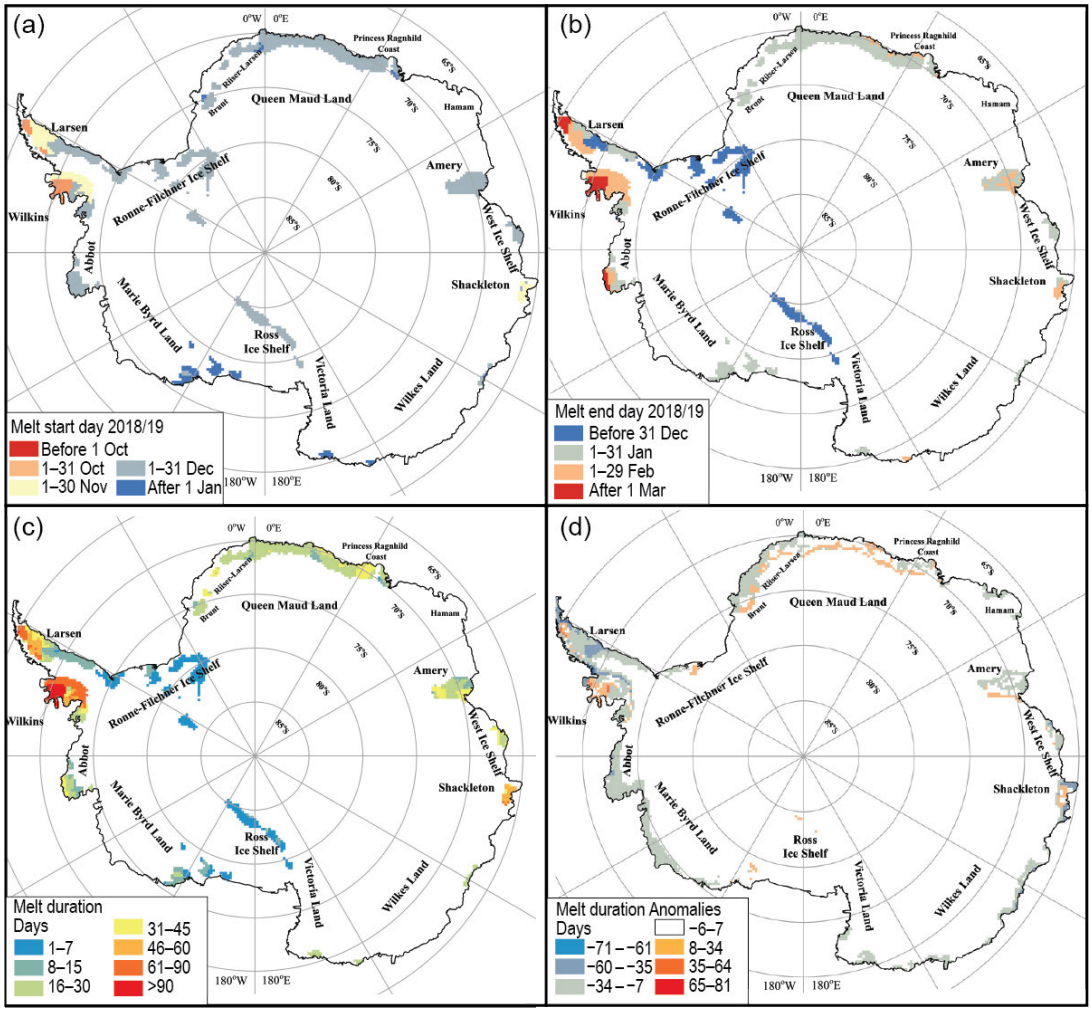

Fig. 6.7. Estimated surface melt for the 2018/19 austral summer: (a) melt start day, (b) melt end day, (c) melt duration, and (d) melt duration anomalies (day) relative to the 1981–2010 mean.

compute surface melt at a spatial resolution of 25 km. The data were preprocessed and provided by the U.S. National Snow and Ice Data Center (NSIDC) at level-3 EASE-Grid format (Armstrong et al. 1994) and were analyzed using a wavelet transform-based edge detection method (Liu et al. 2005). The wavelet transform detects for every satellite pixel the abrupt change in brightness temperature when melt first commences and when melt ends (and freezing commences).

Figure 6.7 shows (a) the start day of the melt season and (b) the end day of the melt season during austral summer 2018/19. The melt duration map shows the total number of melt days at each grid cell location during the melt season (Fig. 6.7c). The melt anomaly map (Fig. 6.7d) is in reference to the 30-year mean (1981–2010).

The earliest melt occurred in October 2018 on portions of the Larsen and Wilkins Ice Shelves (east and west of the Antarctic Peninsula, respectively), which continued into November. Surface melting elsewhere began in November on the Shackleton Ice Shelf in East Antarctica. This extended to the Queen Maud Land coast and Amery Ice Shelf, with brief events on the Ronne and Ross Ice Shelves, which ended by late December (Figs. 6.7a,b). Melt events lasted longer on the Larsen, Wilkins, and Abbot Ice Shelves, i.e., through February and March of 2019, and on the Amery and Shackleton Ice Shelves until February 2019 (Fig. 6.7b).

Ice shelves with longer total melt season duration (>45 days; Fig. 6.7c, orange-red color) include Larsen, Wilkins, and Shackleton (Fig. 6.7c). Areas with moderate melt duration (14–45 days; Fig. 6.7.c, green-yellow color) include the coast of Queen Maud Land and the Abbot and Amery Ice Shelves, while sporadic short-term melt (<16 days; Fig. 6.7c, blue color) occurred on the Ross and Ronne-Filchner Ice Shelves. The melt anomalies (Fig. 6.7d) show that the melt season was generally within ±34 days of the 1982–2010 mean, except for a few small areas on Wilkins Ice Shelf. Therefore, the austral summer of 2018/19 is classified as a low-melt year overall.

Trends in both melt extent (ME) and melt index (MI; Zwally and Fiegles 1994; Liu et al. 2006) show high variability and a general trend toward less melting in the satellite record (since 1978). Melt extent (in km^2) is the total area that experienced surface melt for at least one day during the melt season. The MI (in day·km^2) is the sum of the daily MEs for Antarctica for the entire season. The 2018/19 melt season continued the negative trends observed since 1978 (Fig. 6.8). Both ME and MI trends are significant at $p < 0.05$. Melt extent has decreased by 17 700 km^2 per year and MI has decreased by 322 300 day·km^2 per year over the 43-year record. The 2018/19 austral melt season had the seventh-smallest ME and the third-smallest MI in the satellite record. The negative trends are consistent with our previous reports (Liu et al. 2006; Tedesco 2009a,b). We also note that a majority of the surface melting generally occurs along the Antarctic Peninsula, but a recent weakening of warming trends there (Turner et al. 2016) has contributed to the downward trend in total ME (e.g., Fig. 6.8).

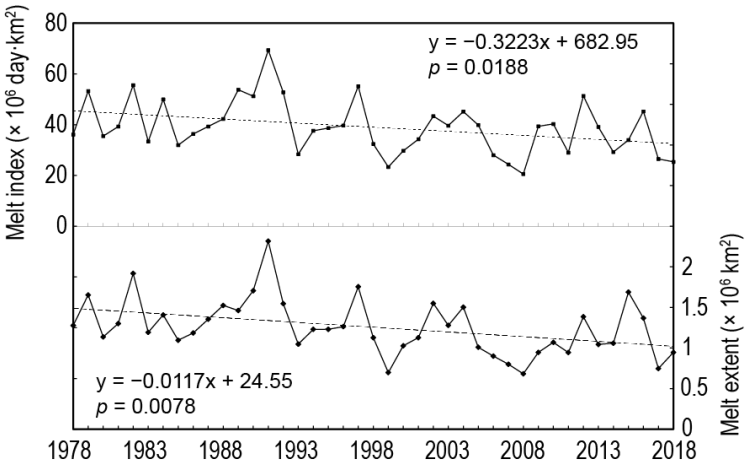

Fig. 6.8. Upper panel: Melt index (×10^6 day·km^2) from 1978/79 to 2018/19, showing a negative trend (322 300 day·km^2 yr^{-1}, $p < 0.05$%). Lower panel: Melt extent (×10^6 km^2) from 1978/79 to 2018/19, showing a negative trend (11 700 km^2 yr^{-1}, $p < 0.05$%). A record low melt was observed during 2008/09. The year marked on the x-axis corresponds to the start of the austral summer. For example, 2008 corresponds to austral summer of 2008/09.

Sidebar 6.2: **Recent changes in the Antarctic ice sheet**—H. A. FRICKER AND A. S. GARDNER

In recent decades the Antarctic Ice Sheet (AIS) has experienced a rapid increase in grounded ice discharge to the ocean. This increase is largely driven by changes in ocean-driven melting and ice shelf thinning.

The AIS gains mass through snowfall (section 6c) and exports mass primarily via two processes at the margins: iceberg calving (episodic) from the ice fronts and basal melting (continuous) under ice shelves (Lazarra et al. 1999; Depoorter et al. 2013). The net balance between competing mass transfers depends on interactions between ice, ocean, and atmosphere. Averaged over long time scales, the contributions from these mass loss processes occur in approximate equal proportions (Rignot et al. 2013), and their sum offsets the mass gain to maintain AIS in steady state. However, since 1992, many ice shelves have experienced net mass loss due to ocean-driven basal melting in excess of the steady state (Adusumilli et al. 2020). after "pushed the ice sheet balance negative" values, which has pushed the ice sheet mass balance negative The SAM index reached its largest negative mean monthly value of the year in November of –4.42 (2nd lowest for November on record since 1957). Major tabular calving events occur on long time scales (50–70 years), and since 1992 there have been major calving events on several ice shelves: Ross (March and April 2000), Ronne (October 1998, May 2000), Larsen-C (July 2017), Pine Island (years), and Amery (September 2019). There have also been several climate change-related collapse events of Antarctic Peninsula ice shelves: Larsen A (January 1995), Larsen B (March 2002), and Wilkins (February–July 2008). These are not cyclical, but represent semi-permanent adjustments of ice shelf extent in light of warmer temperatures and increased melt.

Observing changes in AIS mass is challenging because it is vast and the signals are small, requiring accurate and consistent measurements over a wide range of spatial and temporal scales. Three independent satellite-based techniques are used to estimate AIS mass changes: (a) gravimetry, based on the GRACE and GRACE-FO satellites (e.g., Chen et al. 2009; Velicogna et al. 2009, 2020), which directly measure changes in ice sheet mass at coarse spatial scale (~300 km) in successive satellite passes, but cannot detect changes in floating ice; (b) mass budget method (MBM), which uses estimates of ice velocity and thickness to determine the amount of solid ice that passes across the grounding line and subtracts these against estimates of total snow accumulation over the outlet glacier catchments as determined from atmospheric reanalyses (Gardner et al. 2018; Rignot et al. 2019); and (c) satellite altimetry using either radar or laser altimeters that measure ice sheet surface elevation change over time, combined with model output of changing snow and firn density (that lead to elevation changes without a change in mass) to infer mass changes (e.g., Shepherd et al. 2019; Smith et al. 2020).

Satellite radar (since 1992) and laser altimetry (since 2003) have provided evidence for widespread elevation loss of outlet glaciers in West Antarctica (Pritchard et al. 2009; Wingham et al. 1998), particularly in the Amundsen Sea sector (Pritchard et al. 2012; Shepherd et al. 2001). Soon after the launch of NASA's GRACE satellites in 2002, these data confirmed that the perimeter of the ice sheet was losing mass (Chen et al. 2009; Velicogna 2009) and later revealed evidence of an acceleration in rates of loss (Velicogna et al. 2014). Early application of the MBM (Rignot et al. 2008) confirmed large West Antarctic losses

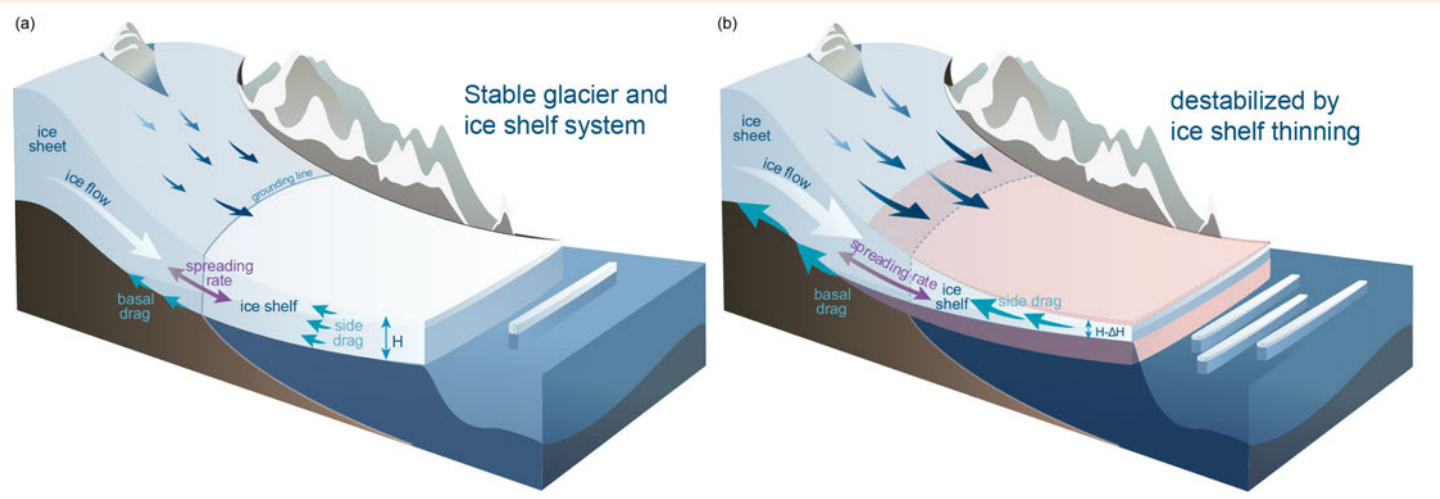

Fig. SB6.2. Schematic showing relationship between ice shelf buttressing and grounding line flux before (a) and after (b) the occurrence of ice shelf thinning. (Figure adapted from Gudmundsson et al. 2019.)

that can be largely attributed to accelerated flow of the Pine Island and Thwaites Glaciers (Gardner et al. 2018; Rignot et al. 2019). Estimates disagree on the sign of recent mass change across East Antarctica, where small changes in net accumulation may greatly impact the net balance (because of its large area). However, the magnitude of the disagreement there is smaller than the mass loss signal elsewhere on the ice sheet.

It can be misleading to directly compare independent published estimates from the three techniques, because they are generally made over different time periods. Recognizing this, a community Ice-sheet Mass Balance Inter-comparison Experiment (IMBIE) was established in 2011 to reconcile estimates for 1992 to 2011 as part of an assessment of the cryosphere for the Intergovernmental Panel on Climate Change (IPCC) Fourth Assessment Report. This showed broad agreement among the three techniques for periods of overlapping measurement and concluded that the ice sheet had an overall negative mass balance (71 ± 56 Gt yr^{-1}; Shepherd et al. 2012). IMBIE2 (IMBIE Team 2018) updated the mass change time series through 2017 and showed that Antarctica lost mass at an average rate of 109 ± 56 Gt yr^{-1} between 1992 and 2017. The rates of ice loss from West Antarctica increased by a factor of three (from 53 ± 29 Gt yr^{-1} during 1992–97 to 159 ± 26 Gt yr^{-1} during 2012–17); from the Antarctic Peninsula, the rate increased from 7 ± 13 Gt yr^{-1} to 33 ± 16 Gt yr^{-1}, in part due to accelerated discharge from outlet glaciers after several ice shelf collapse events. IMBIE2 and Shepherd et al. (2019) also showed that inland thinning is becoming more widespread.

ICESat laser altimetry (2003–08) showed that elevation changes in grounded ice are linked to ocean-driven ice shelf thinning (Pritchard et al. 2009, 2012). The largest thinning rates were observed for coastal West Antarctica, attributed to an enhanced upwelling of warmer Circumpolar Deep Water (CDW) driven by increased westerly winds at the continental shelf break that promoted enhanced melting at depth near the grounding zone of the largest glaciers (Thoma et al. 2008; Steig et al. 2012; Holland et al. 2019). This reduces ice shelf "buttressing", i.e., the back-stress that an ice shelf exerts on the seaward flow of grounded ice behind it (Thomas 1979; Fig. SB6.2). Subsequent analysis of an 18-year (1994–2012) altimetry record from four radar altimeter missions concluded that Antarctic ice shelves are thinning at an accelerating rate, and that their volume has declined by 166 ± 48 km^3 yr^{-1} between 1994 and 2012 (Paolo et al. 2015).

A recent study (Smith et al. 2020) differenced laser altimetry data from NASA's ICESat (2003–09) and ICESat-2 (2018–19) laser altimeters to estimate the mass change over Antarctica's grounded ice sheet and floating ice shelves from 2003 to 2019. The comparison showed pervasive mass loss in both West Antarctica and the Antarctic Peninsula, partially offset by mass gains in East Antarctica; overall, losses outpaced gains, resulting in a net grounded ice mass loss of 118 Gt yr^{-1} for Antarctica (adding a total of 5.2 mm to sea level). In West Antarctica and the Antarctic Peninsula, mass loss from the ice shelves accounted for more than 30% of those regions' total loss, reinforcing the notion of a strong link between ice shelf thinning and loss of grounded ice (Fig. SB6.3). The highest ice shelf thinning rates were in Thwaites Glacier basin in the Amundsen Sea sector.

Early analysis of GRACE-FO satellite gravimetry, combined with GRACE data, shows reduced acceleration of grounded ice loss (i.e., a leveling off) since 2016 (Velicogna et al. 2020). This leveling off stems from an increase in accumulation in Queen Maud Land, George VI land, and the Antarctic Peninsula since 2016. Glacier losses for the Amundsen Sea sector and Wilkes Land were approximately constant since ~2009.

We anticipate that annual assessments of Antarctic mass balance will be available for future *State of the Climate* reports, likely derived from NASA's satellite gravimeter (GRACE-FO) and laser altimeter (ICESat-2).

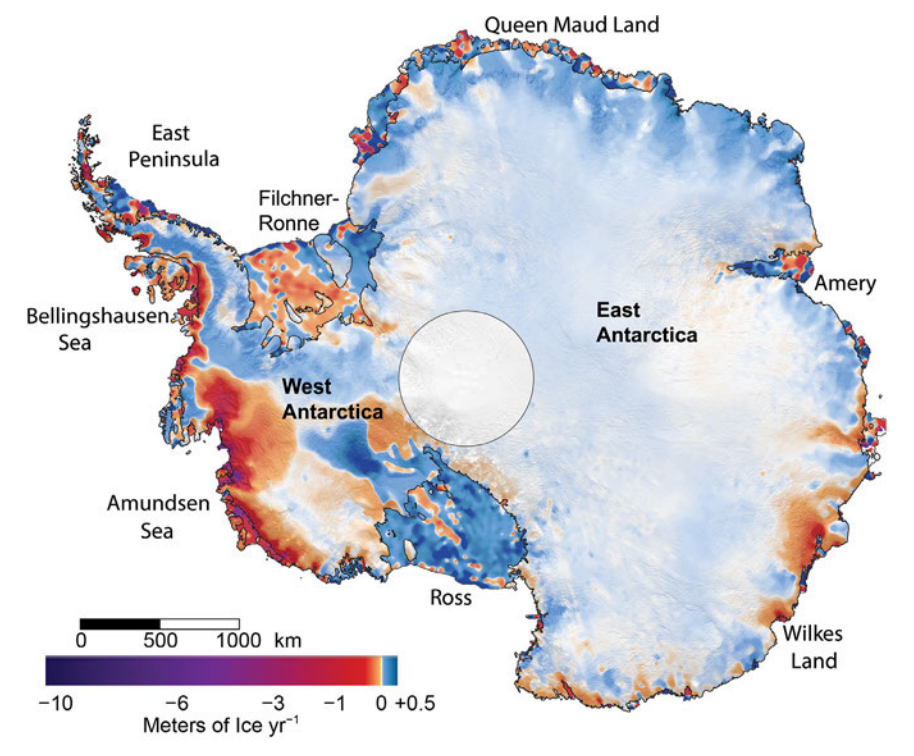

Fig. SB6.3. Mass change of floating and grounded ice (top) from ICESat (2003–09) and ICESat-2 (2018–19) data. (Figure adapted from Smith et al. 2020.)

e. Sea ice extent, concentration, and seasonality—P. Reid, S. Stammerjohn, R. A. Massom, S. Barreira, T. Scambos, and J. L. Lieser

Antarctic sea ice plays a pivotal role in the global climate system. Forming a highly reflective, dynamic, and insulative blanket that varies seasonally in its areal coverage from ~3 × 10^6 km^2 to ~19–20 × 10^6 km^2, sea ice and its snow cover strongly modifies ocean–atmosphere fluxes and interaction processes (Bourassa et al. 2013). Moreover, brine rejection into the underlying ocean during sea ice formation on some continental shelf areas leads to the formation of Antarctic Bottom Water that contributes to the global ocean overturning circulation (Johnson 2008). Antarctic sea ice also acts as a protective buffer for ice shelves against destructive ocean swells (Massom et al. 2018) and modulates the interaction of warm ocean waters with ice shelf basal cavities to affect basal melt there (Timmermann and Hellmer 2013). Finally, it also forms a key habitat for a myriad of biota—ranging from microorganisms to whales (Thomas 2017)—that are strongly affected by changes in the presence and seasonal rhythms of the sea ice cover (e.g., Massom and Stammerjohn 2010).

To place 2019 in context, net Antarctic sea ice extent (SIE, the area enclosed by the ice edge consisting of ≥15% sea ice concentration [SIC]) showed a slight increasing trend over 1979–2015 (Comiso et al. 2016) that was then marked by increased interannual variability since 2012. Record high SIE values during 2012–14 (Reid and Massom 2015) were followed by record lows from 2016 through 2019 (Figs. 6.9a,c). The persistent record-breaking low SIE since 2016 suggests a response to a change in the underlying ocean conditions (Meehl et al. 2019), particularly for the

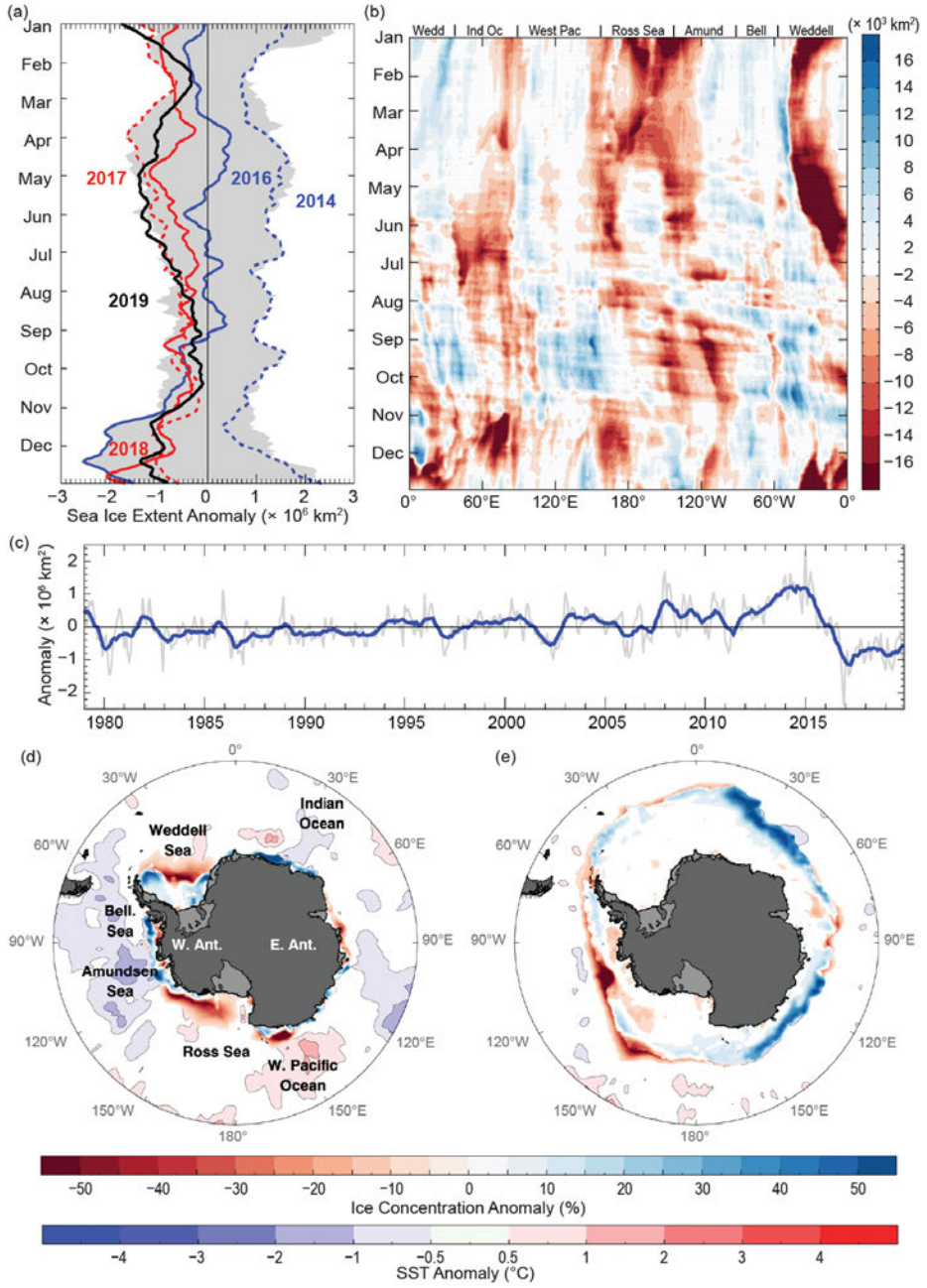

Fig. 6.9. Antarctic sea ice in 2019. (a) Time series of net SIE anomalies for 2014 (dashed blue line), 2016 (solid blue line), 2017 (dashed red line), 2018 (solid red line), and 2019 (solid black line) (all relative to the 1981–2010 climatology). Gray shading represents the historical range (1979–2018) in SIE anomalies. (b) Hovmöller (time–longitude) representation of SIE anomalies (× 10^3 km^2 per degree of longitude) for 2019. (c) Time series (1979–2019) of monthly average SIE anomalies (light blue) and their 11-month running mean (dark blue). Maps of SIC anomaly (%) and SST anomaly (°C) for (d) Feb and (e) Sep 2019 (all relative to 1981–2010). Sea ice concentration is based on satellite passive-microwave ice concentration data.

Ross Sea and western Weddell Sea (Fig. 6.9b; Reid et al. 2018, 2019). Also persistent over the last few years (from mid-2017 through 2019) are positive anomalies in both SIE (e.g., Fig. 6.9a) and duration (e.g., Fig. 6.10c) in the eastern Amundsen and Bellingshausen Seas (ABS) region. These persistent positive SIE anomalies could be the result of enhanced sea ice melt (Haumann et al. 2020) together with regional freshening of the upper ocean from observed enhanced melting of Thwaites Glacier and the adjacent outlet glaciers (Bintanja et al. 2013; St-Laurent et al. 2017). Below-normal sea surface temperatures (SSTs) were also observed more frequently off the ABS region since 2017 (e.g., Fig. 6.9d). This region previously showed strong decreases in both sea ice coverage and duration over 1979–2014 (Fig. 6.10d; Stammerjohn et al. 2015).

Highlights from 2019 include record low monthly mean SIE recorded in both January and June (Fig. 6.9a), with 59 record low daily values of SIE also occurring in January, May, June, and July. Indeed, net SIE was below the long-term average (1981–2010) for all days in 2019 (Fig. 6.9c), with 11 days (all in January) also showing the lowest sea ice area (SIA; the actual area covered by sea ice) on record (not shown). The annual daily minimum SIE for 2019 occurred on 28 February (at 2.44×10^6 km^2, the seventh lowest on record), while the daily maximum was on 30 September (18.46×10^6 km^2, 10th lowest on record).

In addition to these highlights, Antarctic sea ice coverage during 2019 was characterized by high spatial and seasonal variability, consistent with variability in the overlying atmospheric and underlying oceanic conditions. The seasonal and regional progression of SIE anomalies during the year can be broken into four phases based on spatio-temporal analysis (Fig. 6.9b): January–February; March–June; July–mid-October; and mid-October–December. These four phases of SIE anomaly patterns are described below, together with associated atmospheric and/or oceanic features drawn from sections 6b and 6g, respectively.

The net circumpolar SIE at the start of 2019 was at record low values until about mid-January, after which the negative net circumpolar SIE anomaly weakened into mid-February (though remained negative; Fig. 6.9a). During this time, a distinct and persistent zonal wave-3 pattern was observed in the regional SIE anomalies (Fig. 6.9b), despite a

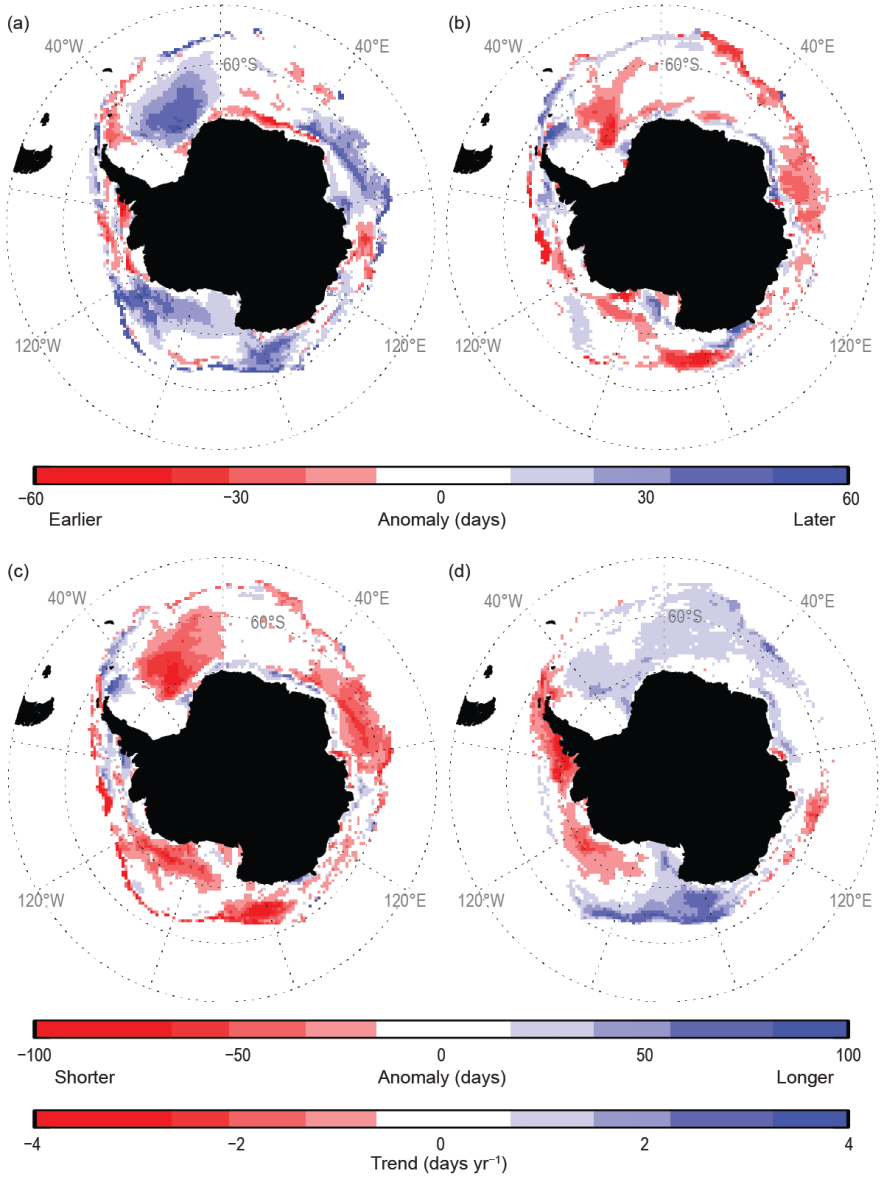

Fig. 6.10. Antarctic sea ice seasonality in 2019. Maps showing 2019 anomalies of days of (a) advance and (b) retreat, (c) total duration, and (d) duration trend (following Stammerjohn et al. 2008). Both the climatology (for computing the anomaly) and trend are based on 1981/82–2010/11 data (Cavalieri et al. 1996 [updated yearly]), while the 2019/20 duration-year data are from the NASA Team NRTSI dataset (Maslanik and Stroeve 1999).

prevalent zonal wave-2 pattern in atmospheric pressure (section 6b; Fig. 6.3a). Dominant factors during this initial period were strong and persistent negative SIE anomalies in: (1) the eastern Indian Ocean; (2) the eastern side of the west Pacific through to the Ross Sea and western Amundsen Sea sectors; and (3) the western Weddell Sea. The weakening of negative circumpolar SIE anomalies in February coincided with a weakening of the strong positive SIE anomalies across extensive parts of the ABS, western Indian Ocean (~0°–50°E), and western Pacific Ocean (~90°–150°E), which also coincided with negative SST anomalies immediately north of the ice edge (Fig. 6.9d).

The short-lived period of near-average circumpolar SIE in February rebounded to become strongly negative again, resulting in record negative anomalies in May–June (Fig. 6.9a). This stalling of the annual autumn sea ice advance was dominated by strong negative anomalies in the Ross and western Weddell Seas and the eastern Indian Ocean sector (Figs. 6.9b, 6.10a). These regional negative anomalies effectively overrode lower-magnitude positive SIE anomalies in the intervening eastern Weddell Sea–western Indian Ocean, western Pacific Ocean, and eastern ABS sector. As the autumn sea ice advance progressed, a major low-pressure system to the north of the Ross Sea during April led to an abrupt change to greater-than-average ice formation and ice-edge advance in the central Ross Sea (~150°W–180°) starting in mid-April. Contemporaneously, there was a westward zonal broadening of the negative SIE anomaly in the Indian Ocean sector and an intensification of the western Weddell Sea negative anomaly.

During July, sea ice coverage expanded rapidly in the western Weddell Sea and to a lesser extent in the central Ross Sea, which was likely a delayed response to June's strong atmospheric anomalies (Fig. 6.3c) and an associated increase in westerly winds (Fig. 6.2c) near the sea ice edge. Meanwhile, the major negative anomalies in the Indian Ocean and the eastern Ross Sea propagated eastward. In August through the end of September, the strong negative net SIE anomaly again weakened (though still remained negative), with above-normal SIE within the eastern Weddell to western Indian Ocean sector (~10°–50°E), the western Pacific (~110°–150°E), and (to a lesser extent) in the Bellingshausen to western Weddell Seas sector (~60°–90°E; Fig. 6.9e).

From mid-October onward, there was another sudden decrease in net SIE (Fig. 6.9a). Anomalously early seasonal retreat extended eastward from ~30°W to ~130°E, and within the western Ross Sea and Amundsen Sea, to persist through the end of the year (Fig. 6.10b). These regional sea ice decreases were in response to substantial changes in atmospheric forcing (Figs. 6.2, 6.3 and Sidebar 6.1). Part of those changes involved increased cyclogenesis to the south of South Africa caused by enhanced Rossby wave activity associated with a strengthening of the Indian Ocean dipole (IOD; e.g., as described by Yuan et al. 2018; see also section 4h). Antarctica also experienced a strong stratospheric warming at this time (Sidebar 6.1), which led to an overall decline in the strength of the dominant westerly wind field.

In terms of annual ice season duration (ISD; February–February, Fig. 6.10c), 2019/20 was overall quite a departure from the long-term linear trends (Fig. 6.10d). This is particularly the case in the western Weddell Sea and the Ross Sea, where long-term trends since 1979 have been positive, in contrast to the distinctly negative ISD anomalies in 2019 (Figs. 6.10c,d). Similarly, the positive 2019 ISD anomalies in the Bellingshausen and northwestern Weddell Seas were also in marked contrast to the observed strongly negative long-term trends there. For ISD, the only area consistent with the long-term trend was the eastern Ross Sea to western Amundsen Sea region.

f. Southern Ocean—B. Y. Queste, E. P. Abrahamsen, M. D. du Plessis, S. T. Gille, L. Gregor, M. R. Mazloff, A. Narayanan, F. Roquet, and S. Swart

To quantify changes in shelf regional temperature anomalies, we assess Southern Ocean 2019 anomalies in the context of the past two decades from conventional ship-based campaigns and from the Marine Mammals Exploring the Oceans Pole to Pole (MEOP) database, the latter illustrating the capabilities of animal-borne sensors. We then analyze 2019 data illustrating the importance and variability in both heat and carbon flux anomalies at the surface of the Southern Ocean over seasonal time scales.

1) Variability in the decline of Antarctic bottom water volume

Several studies have described warming and freshening of deep and bottom water layers in the Weddell and Ross Seas (Jullion et al. 2013; Jacobs and Giulivi 2010) and in basins farther north (Desbruyères et al. 2016; Menezes et al. 2017; Purkey and Johnson 2013; Purkey et al. 2019), along with a decrease in the volume of the densest bottom waters (Purkey and Johnson 2012). However, recent repeat hydrographic measurements have shown that the volume of Weddell Sea Bottom Water has increased from 2014 to 2018 (Fig. 6.11a; Abrahamsen et al. 2019), while measurements in the Ross Sea show a rebound in salinity of shelf waters that form precursors to Ross Sea Bottom Water (Castagno et al. 2019). These are the first observations suggesting a deviation from a monotonic decline in volume and salinity in recent years.

Salinity decreases in the Ross Sea shelf waters have been attributed to changes in sea ice and increased basal melting of ice shelves in the upstream Amundsen Sea (Jacobs and Giulivi 2010). In contrast, trends in Weddell Sea Bottom Water have been smaller, though also showing a decreased salinity through the 2010s, with a subsequent increase since 2016 (Gordon et al. 2020). With both regions affected by large-scale climate modes (e.g., Southern Annular Mode [SAM] and El Niño–Southern Oscillation [ENSO]), albeit through different mechanisms (e.g., Gordon et al. 2020; McKee et al. 2011; Paolo et al. 2018; Steig et al. 2012), it remains to be seen if the recently observed variations are merely a temporary lull in a longer-term trend or not.

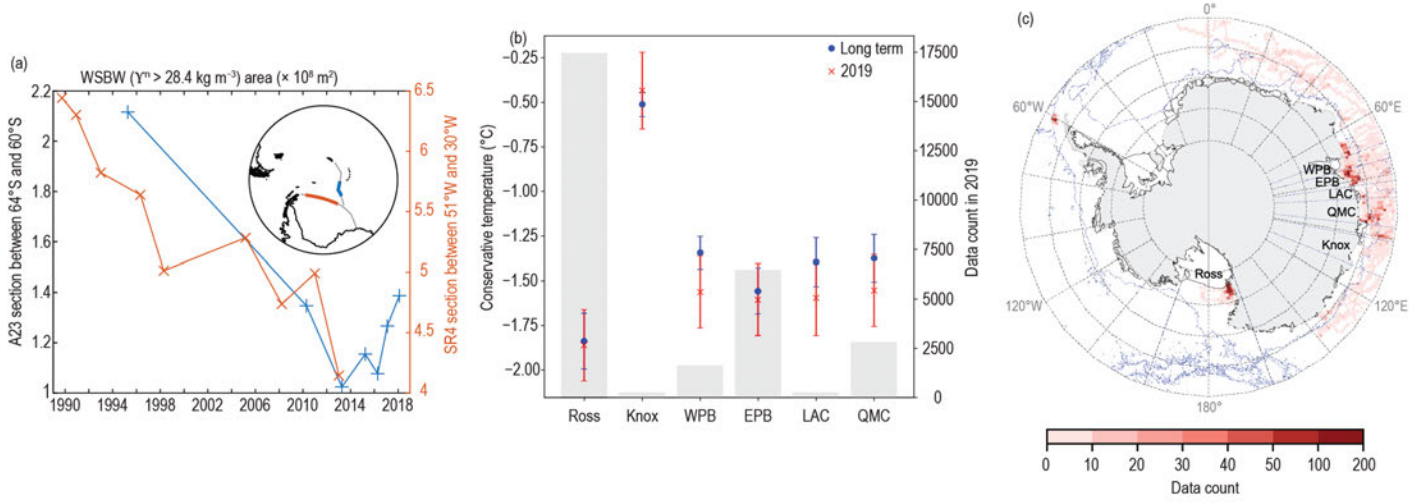

Fig. 6.11. Southern Ocean abyssal and coastal anomalies in 2019. (a) Areas of Weddell Sea Bottom Water water masses on hydrographic sections. (b) Mean conservative temperatures for depths below 250 m. Averages are taken for each region using profiles at least 75 km from the coast or ice shelf edge and where depths are shallower than 3000 m (i.e., only over the continental shelf; the 3000-m bathymetry contour is shown in blue). The blue meridional lines denote the boundaries of each analysis region. Gray bars denote the data count (on the right axis) of 2019 data. Region names along the x axis are: Ross Sea (Ross, 160°E–160°W): Knox Coast (Knox, 101°–112°E); western Prydz Bay (WPB, 70°–75°E); eastern Prydz Bay (EPB, 75°–82°E); Leopold and Astrid Coast (LAC, 82°–87°E); and Wilhelm II Coast and Queen Mary Coast (QMC, 87°–96.5°E). Red denotes 2019 data, and blue denotes 2004–17 data. The whiskers are the combined nominal instrument error and the standard error of the mean measurements within the box. For more on the methods see Narayanan et al. (2019). (c) Data count for the year 2019 aggregated in grid cells of 0.5° × 0.5° cells.

2) Ocean temperatures on the Antarctic continental shelf from animal-borne sensors

The 2004–17 MEOP data (Roquet et al. 2014; Treasure et al. 2017) offer a means to investigate Antarctic shelf water masses. Narayanan et al. (2019) showed that the presence of dense shelf waters coincides with an absence of warmer Circumpolar Deep Water. As part of that study, mean temperatures were quantified at depths ranging from 250 m to the bottom, and from the coast or ice shelf edge (75 km and beyond) to the continental shelf and slope (shallower than 3000 m). Here we take the available 2019 MEOP data and repeat that analysis (Fig. 6.11b). In 2019, there were two regions with relatively good data coverage (Fig. 6.11c): the coastal areas off Princess Elizabeth Land and the Ross Sea (Ross). The observed 2019 Antarctic shelf temperatures are, on average, slightly lower than the 2004–17 temperatures in almost all the regions investigated, although the difference is not statistically significant (Fig.6.11b). This result, implying somewhat stable temperatures on the Antarctic shelf, demonstrates that MEOP-CTD data now enable us to monitor a large portion of this sensitive and climatically impactful region.

3) Surface heat fluxes

We use NCEP-II reanalysis data (Kanamitsu et al. 2002) to evaluate the seasonal and annual state of the surface net heat flux in 2019 compared with the 1981–2010 climatology south of 35°S. Positive values denote a heat flux into the ocean. We note that there remains large inter-product spread in net heat flux estimates in the Southern Ocean (Liu et al. 2011; Josey et al. 2013; Swart et al. 2019) with no consensus on which product best represents Southern Ocean conditions. NCEP-II, however, is considered a robust global heat flux product.

The 2019 anomaly (Fig. 6.12c) shows mostly positive values (10–40 W m^{-2}), particularly in the Indian and Pacific sectors of the Antarctic Circumpolar Current (ACC), with weak positive anomalies in the Atlantic. The mean net heat flux over the Southern Ocean during 2019 was 4.8 W m^{-2} larger than the climatological mean, the largest yearly-averaged positive difference over the last 30 years (Fig. 6.12a). We also note the general upward trend in annual heat flux since the late 1990s and the positive atmosphere-to-ocean heat flux every year since 2010. Large negative

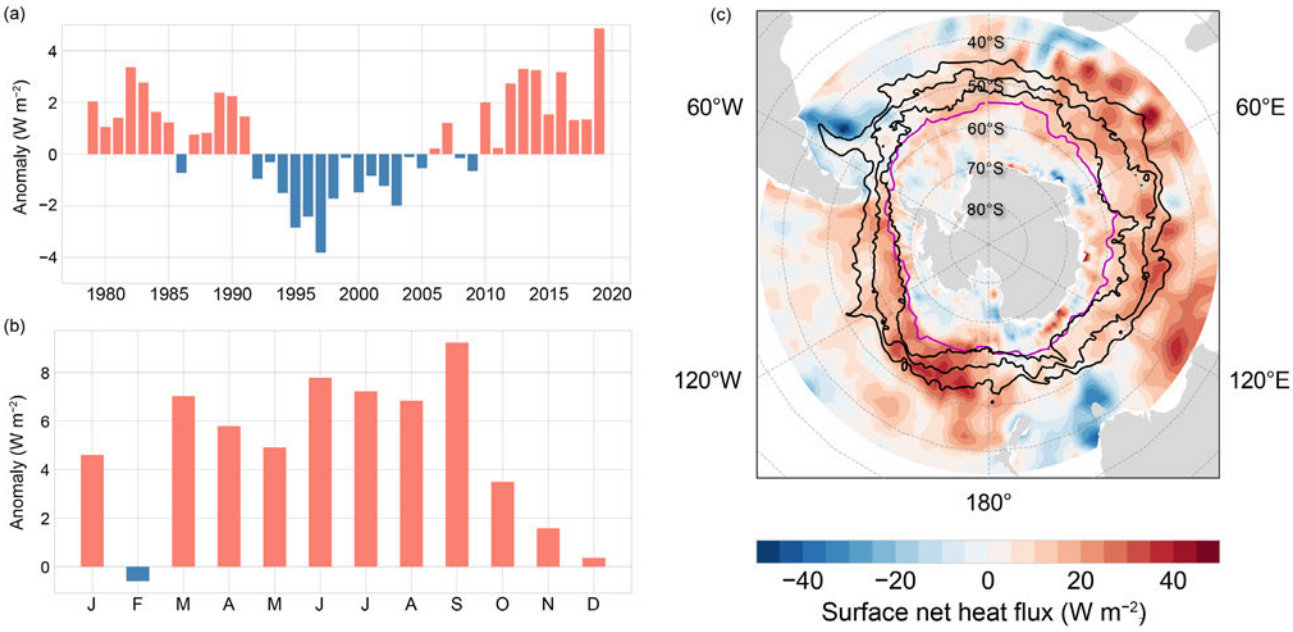

Fig. 6.12. (a) 30-year time series of heat flux anomalies for the Southern Ocean south of 35°S from NCEP-II reanalysis data. (b) Monthly net heat flux anomalies during 2019 south of 35°S. (c) The mean surface net heat flux (positive denotes into the ocean; in W m^{-2}) anomaly for 2019 (minus the 30-year climatology) from NCEP-II reanalysis data. The main ACC fronts are depicted as black contours, from north to south, as the Subantarctic Front and the Antarctic Polar Front from AVISO Mean Absolute Dynamic Topography (as in Swart et al. 2010), while the maximum SIE (15% SIC from NCEP/DOE AMIP-II Reanalysis) is shown as the magenta contour.

anomalies (–20 W m^{-2}) were confined to the confluence of the northern ACC boundaries and western boundary currents south of Africa, Tasmania, and the Falklands. The seasonal ice zone did not, on average, experience any significant heat flux anomalies during 2019. The 2019 monthly heat flux anomalies (Fig. 6.12b) were positive in all months except February (–0.6 W m^{-2}). Autumn to winter anomalies (March–September) are significantly more positive (4.9 to 9.2 W m^{-2}), with a maximum in September. It is uncertain why such positive anomalies exist in autumn–winter, but they may be associated with anomalies of surface air temperature and with the phase and intensity of the SAM index during 2019 (Figs. 6.2c, 6.3).

4) Surface CO_2 fluxes

Over the last five years, floats have increased the number of perennial CO_2 flux observations in the Southern Ocean (Johnson et al. 2017; Williams et al. 2017). Bushinsky et al. (2019) incorporated these float data into a neural network approach to predict surface CO_2 fluxes (MPI-SOMFFN by Landschützer et al. 2016), affirming that the Southern Ocean sink may be ~35% weaker than previously estimated (Gray et al. 2018). The interannual comparison is done using an adaptation of the CSIR-ML6 method that incorporates the available Southern Ocean Carbon and Climate Observations and Modeling (SOCCOM) project's float data (Gregor et al. 2019).

Estimates of the net flux of CO_2 (FCO_2) show that there was a statistically insignificant decrease in the Southern Ocean sink when comparing 2016–18 with 2019 (–0.63 Pg C yr^{-1} to –0.62 Pg C yr^{-1}, respectively). This variation does not contradict the findings by Keppler and Landschützer (2019) who found a weakening Southern Ocean sink from 2012. A seasonal breakdown shows that differences in winter and spring were zonally consistent compared with summer and autumn (Fig. 6.13). Winter showed weaker CO_2 sources in the Atlantic and Indian sectors but a stronger CO_2 source in the central Pacific (Fig. 6.13e). Regional variability is large in summer (Fig. 6.13g), where CO_2 uptake increased in the Atlantic and south of Australia. The increased uptake in summer was likely caused by interannual variability in primary production (Gregor et al. 2018). Finally, in autumn, the eastern Pacific sector became a strong CO_2 source region (Fig. 6.13h).

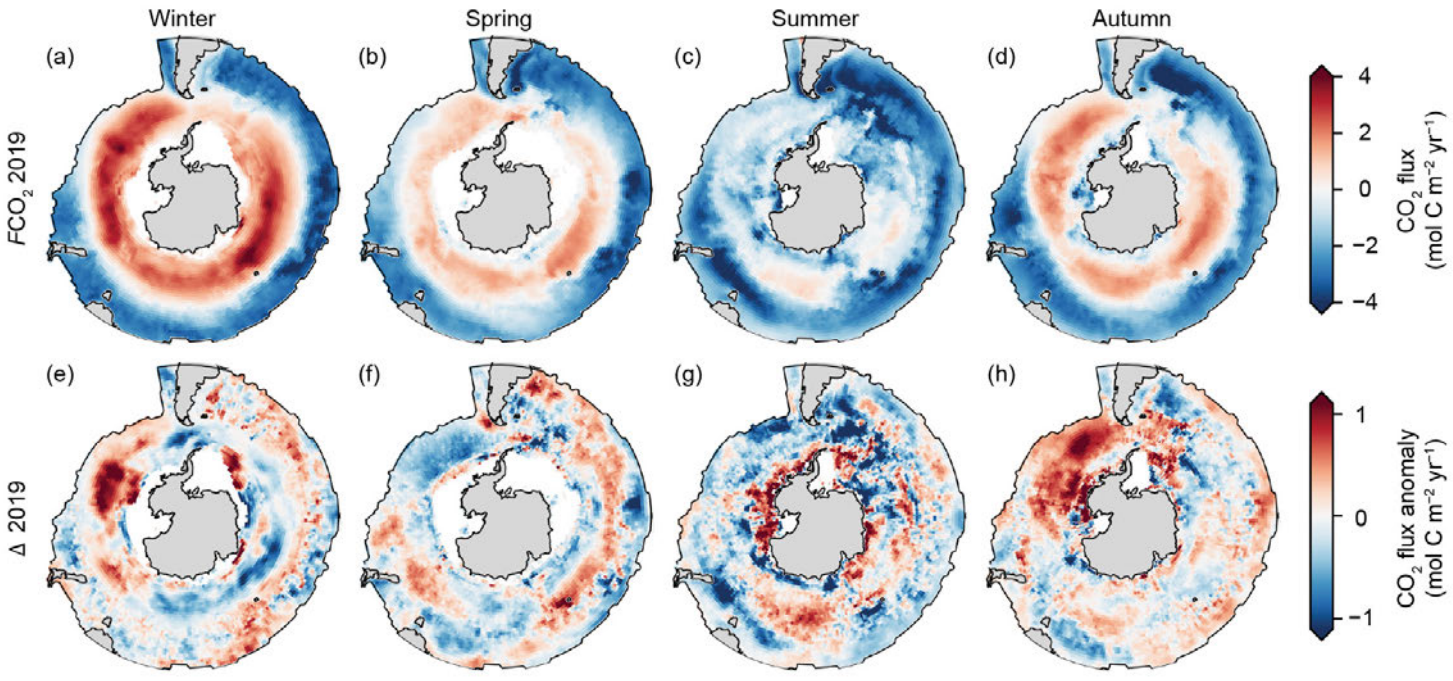

Fig. 6.13. Southern Ocean CO_2 fluxes in 2019. (a)–(d) the total air–sea CO_2 fluxes in 2019 for each of the seasons of FCO_2 between 2019 and the comparison period (2016 to 2018), where positive (red) values are out of the ocean into the atmosphere. (e)–(h) the difference between 2019 and the comparison period (2016–18); blue/red shows less/more CO_2 has exchanged between the ocean and the atmosphere. The maps have been limited to the Southern Ocean region as defined by Fay and McKinley (2014).

g. 2019 Antarctic ozone hole—N. Kramarova, P. A. Newman, E. R. Nash, S. E. Strahan, C. S. Long, B. Johnson, M. Pitts, M. L. Santee, I. Petropavlovskikh, L. Coy, and J. de Laat

The weakest Antarctic ozone hole since the early 1980s occurred in 2019. This weak hole was caused by atypically strong planetary-scale waves that propagated upward from the troposphere (Sidebar 6.1). These waves displaced and weakened the stratospheric polar vortex, slowing the 10-hPa zonal mean wind from 87 m s^{-1} to 11 m s^{-1} between 25 August and 17 September. The increased descent of stratospheric air, associated with the vortex weakening (section 6b and Sidebar 6.1), warmed the stratosphere such that the 2019 September 50-hPa Antarctic temperature was 16 K above average, setting a record for 2019. These unusually above-normal lower stratospheric temperatures reduced polar stratospheric clouds (PSCs) and slowed catalytic ozone depletion.

Strong planetary wave events dominated the 2019 ozone hole evolution and affected ozone in two ways. First, these events forced downward motion in the polar region, bringing ozone down to the lower stratosphere. Second, they increased meridional transport of ozone-rich air from midlatitudes into the Antarctic mid-to-upper stratosphere above the ozone hole (Sidebar 6.1).

Lower stratospheric temperatures increased in mid-August, and by early September, they were well above the 2005–18 average (Fig. 6.14a). This stratospheric warming occurred at the pivotal time for ozone depletion. Substantial Antarctic ozone depletion begins in August during the Southern Hemisphere (SH) late winter as the sun's rays return to polar latitudes, activating

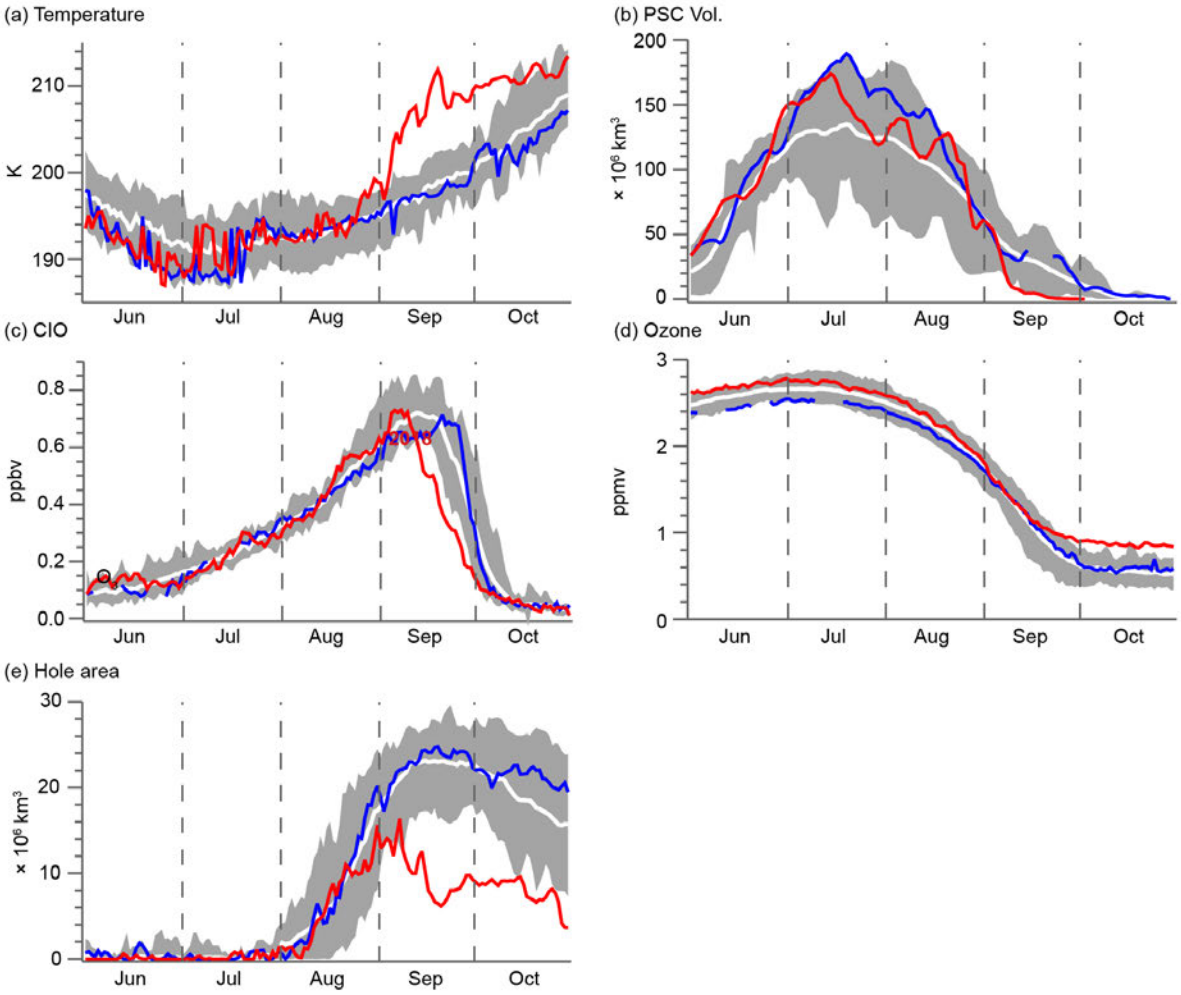

Fig. 6.14. Antarctic 2019 (red curves) and 2018 (blue curves) values of (a) vortex-averaged MERRA-2 temperature (K); (b) CALIPSO PSC volume (× 10^6 km^3; updated from Pitts et al. 2018); vortex-averaged concentrations of (c) ClO (ppbv) and (d) O_3 (ppmv) measured by MLS (updated from Manney et al. 2011); and (e) OMI/OMPS Antarctic ozone hole area (× 10^6 km^3; area with ozone total column less than 220 DU). MERRA-2 temperature and MLS averages are made inside the polar vortex on the 440-K potential temperature surface (~19 km or 60 hPa). Gray shading shows the range of daily values, and the white curves indicate the long-term mean for 2005–18, except for (b) that uses the period 2006–18.

chlorine and bromine chemistry that depletes ozone. PSC particles provide surfaces for heterogeneous chemical reactions that release chlorine and catalytically destroy ozone. The wave events led to earlier-than-usual PSC disappearance over Antarctica (PSC volume dropped to almost zero by mid-September), suppressing ozone depletion far earlier than usual (Fig. 6.14b).

The 2019 chlorine monoxide (ClO) concentrations from the *Aura* Microwave Limb Sounder (MLS) rapidly declined in early September, and by late September they reached the lowest values observed in the 2005–19 record (Fig. 6.14c). ClO is directly related to the rate of ozone depletion. Typically, ClO steadily increases as sunlight returns to Antarctica, and its enhancement continues until mid-October. Because of low ClO in 2019, ozone levels (Fig. 6.14d) in mid-September to October were 13%–55% above the seasonal average. The early August hole area (Fig. 6.14e) grew normally, but growth slowed in late August, reaching its peak extent of 16.4 million km^2 (Mkm^2) on 8 September. It shrank below 10 Mkm^2 by 15 September and remained low through October. In contrast, the 2018 area with lower temperatures and higher ClO was relatively large (Fig. 6.14e, blue curves).

Antarctic total ozone column is determined by two main parameters: abundances of ozone-depleting substances (ODS) and Antarctic lower stratospheric temperatures. The effective equivalent stratospheric chlorine (EESC) is an estimate of the amount of human-made ODS in the stratosphere. EESC has gradually declined from its peak in 2000. The September Antarctic polar cap (60°–90°S) total ozone follows EESC changes (EESC fit shown as magenta in Fig. 6.15b). In 2019, satellite measurements show that polar cap total column ozone had the highest concentrations over the 40-year period (Fig. 6.15b). The 2019 September average of the minimum total ozone values over Antarctica (Fig. 6.15c) was the highest observed since 1988, but not a record high. Antarctic ozone continued an upward trend since 1999, consistent with decreasing stratospheric EESC levels (blue line in Fig. 6.15c).

Dynamical variability in September stratospheric ozone over the South Pole is typically weak, and lower stratospheric ozone partial columns are mostly controlled by the photochemical

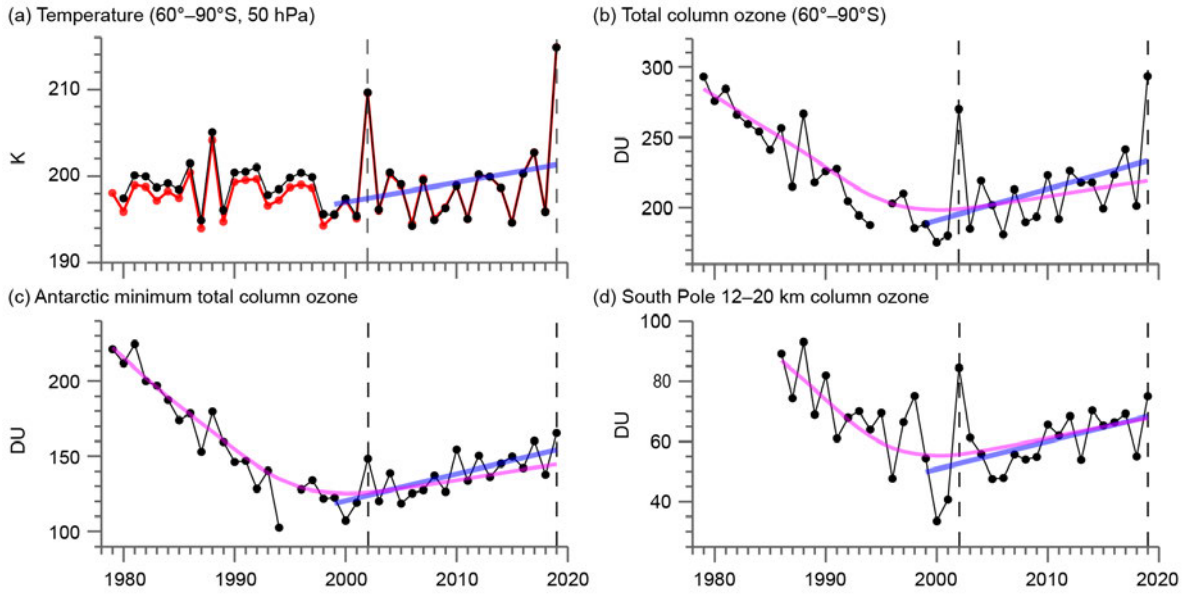

Fig. 6.15. Long-term variability of ozone and atmospheric temperature. (a) 50-hPa Sep mean temperature (K) over 60°–90°S from MERRA-2 (black) and ERA5 reanalyses (red). Note that the ERA5 and MERRA-2 values exhibit a consistent bias for the period up to 1998, but the two datasets are in excellent agreement from 1999 to the present. (b) Sep mean total ozone column (DU) over 60°–90°S and (c) minimum total ozone column over Antarctica derived from NASA satellite sensors (TOMS, OMI, and OMPS). (d) Sep mean partial ozone column (DU) measured within the primary depletion layer (12–20 km) by NOAA South Pole ozone sondes. Blue lines indicate linear trends for the time period 1999–2019. The magenta curve in (b), (c), and (d) is the quadratic fit of ozone columns to effective equivalent stratospheric chlorine (EESC). The vertical lines indicate the anomalous years 2002 and 2019.

depletion rates. The September South Pole ozone partial columns between 12 and 20 km (Fig. 6.15d; derived from NOAA balloon profiles) have higher correlations with Antarctic minimum column ozone than with polar cap averages. In September 2019, the mid-to-upper stratospheric polar vortex was displaced from the South Pole, resulting in large stratospheric temperature and ozone profile variability and anomalies. The lowest 2019 South Pole total ozone was recorded earlier than usual (24 September), with a polar-centered vortex, and the lowest partial column ozone was observed a half month later (10 October). As with the minimum total column ozone, the South Pole partial column ozone shows an upward trend since the late 1990s.

Interannual variations in Antarctic stratospheric temperature influence observed ozone trends. Antarctic ozone anomalies are highly correlated with lower stratospheric temperatures (Fig. 6.16). Anomalies are derived by subtracting a quadratic EESC fit from the observed September mean total ozone over the Antarctic polar cap (black line in Fig. 6.15b). Record high column ozone in 2019 resulted from record high September temperatures (Sidebar 6.1). In 2002, Antarctic ozone rapidly declined until mid-September, when the wave events disturbed the polar vortex and caused rising temperatures. The 1988 and 2017 holes were also small because of higher temperatures, while the 2018 hole was large because of lower-than-average Antarctic temperatures (Fig. 6.15). Strong wave events occurred infrequently in the Antarctic during the past 40 years (Langematz and Tully 2018). When they do occur, the impact from strong wave events, like those observed in September 2002 and 2019 (indicated by vertical dashed lines in Fig. 6.15), are revealed by strong extremes in the observations (Fig. 6.15).

An upward temperature trend contributes to an upward ozone trend (i.e., a shift toward the upper right of Fig. 6.16). There is a non-statistically significant +2.3 K decade^{-1} trend (76% confidence, two-sided test) in the September mean Antarctic lower stratospheric temperature since 1999 (blue line in Fig. 6.15a), with non-significance likely reflecting the short record. Nevertheless, this upward temperature trend adds to observed ozone increases arising from EESC decline (Figs. 6.15b–d). Antarctic polar cap ozone (blue line in Fig. 6.15b) has a +22.3 DU decade^{-1} trend since 1999 (94% confidence). Positive trends are also apparent in the Antarctic minimum column ozone (+17.9 DU decade^{-1} with >99% confidence; Fig. 6.15c) and South Pole observations (+9.2 DU decade^{-1} with 95% confidence; Fig. 6.15d). While declining ODS levels contributed to the smaller 2019 ozone hole, the primary cause was the unusually strong dynamical waves, similar to 2002 conditions.

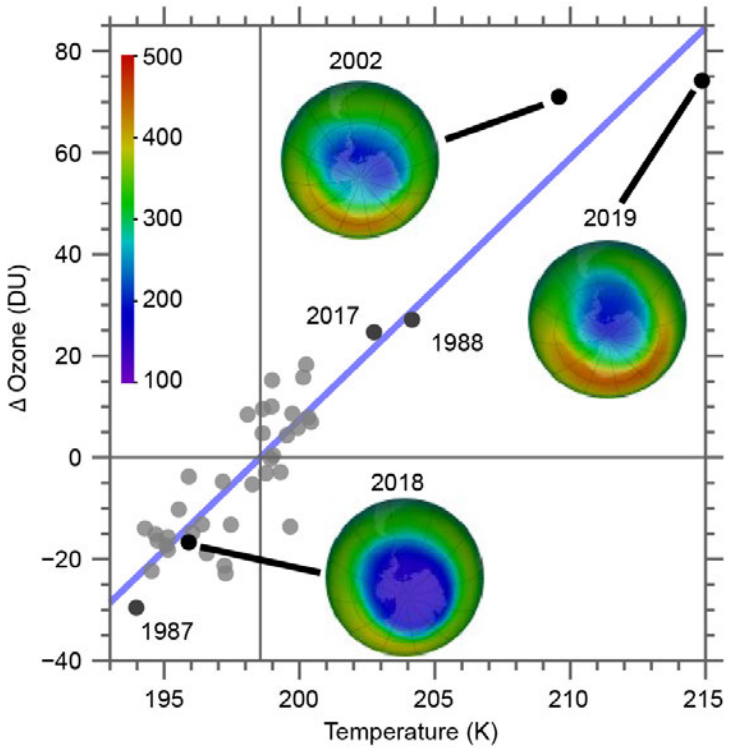

Fig. 6.16. Column ozone anomalies (DU) vs. ERA5 50-hPa Sep mean temperatures (K) in the 60°–90°S region (values from Figs. 6.15a,b). The ozone anomalies for each year are calculated by subtracting a quadratic EESC fit (magenta line in Fig. 6.15b) from the observed Sep mean total ozone over the Antarctic polar cap (black line in Fig. 6.15b). The inset false-color images are Sep mean total column ozone. The horizontal line indicates the zero anomaly for column ozone, while the vertical line indicates the temperature at this zero-ozone anomaly. The blue line shows the linear fit.

SIDEBAR 6.3: Sea Ice Prediction Network-South: Coordinating seasonal predictions of sea ice for the Southern Ocean—J. L. LIESER, F. MASSONNET, W. HOBBS, J. FYFE, C. M. BITZ, AND P. REID

The Sea Ice Predication Network (SIPN) is a community-wide effort to assess seasonal sea ice forecasts for the Arctic. It has been in operation since 2008, when it started life as the SEARCH Sea Ice Outlook (Hamilton and Stroeve 2016). This international initiative has created a strong community of researchers from various backgrounds with a common interest in forecasting sea ice conditions in the Arctic Ocean.

SIPN-South now expands this prediction network by providing seasonal sea ice forecasts for the Southern Ocean. Endorsed by the Year of Polar Prediction project (Jung et al. 2016), SIPN-South provides a focal point for a seasonal forecast of Antarctic sea ice, which is thought to be less predictable than Arctic sea ice. However, recent research (Marchi et al. 2018) suggests that, in fact, the large thermal inertia of the Southern Ocean together with atmospheric teleconnections from outside the immediate Antarctic realm (Pope et al. 2017) could represent the key factors for Southern Hemisphere (SH) sea ice predictability.

Highly variable sea ice extent is one of the many challenges that vessels face when operating in the Antarctic coastal region, and this can substantially impact science, science support, and logistic operations as well as fishing and tourist activities in those regions. These logistical challenges were highlighted during a dedicated workshop held by the Council of Managers of National Antarctic Programs (COMNAP 2015). Advance notice of seasonal sea ice conditions could help reduce risks to the operations and the environment and costs associated with providing alternative operational logistics. In 2017, the provision of sea ice outlooks became even more relevant when the International Maritime Organization's (IMO) International Code for Ships Operating in Polar Waters (known as the Polar Code) came into force (IMO 2017). The Polar Code provides polar ship operators with a framework for mandatory measures as well as recommended provisions covering safety and pollution prevention. One of these measures is voyage planning, which is ideally informed by the best-possible observations of current sea ice conditions but also predictions of conditions in the near- and medium-term future. SIPN-South's key role in this is to provide a forum within which research organizations and individuals may openly discuss their model's performance against other similar endeavours. Hence, the initiative will help inform the development of suitable sea ice forecasting models for the Antarctic.

SIPN-South has now successfully completed two campaigns of solicited Antarctic summer sea ice predictions. These predictions are featured in two published reports that evaluate forecasts against observed sea ice states (Massonnet et al. 2018, 2019). For the summer 2019/20 season, the third installment of the project received 11 submissions at the beginning of December 2019 (Table SB6.1). Figure SB6.4a shows the total

Table SB6.1. Information about contributions to the summer 2019/20 coordinated sea ice forecast experiment. Contributors provided, in order of descending priority: (1) the total Antarctic sea ice area (SIA) for each day of Dec–Feb 2019/20; (2) the SIA per 10° longitudinal band (rSIA) for each day of Dec–Feb 2019/20; and (3) the sea ice concentration (SIC) for each day of Dec–Feb 2019/20.

	Contributor name	Short name (in figures)	Forecasting method	Number of forecasts	Initialization date	Diagnotstics provided
1.	Nico Sun	NicoSun	Statistical model	3	30 Nov	SIA + SIC
2.	NASA-GMAO	nasa-gmao	Coupled dynamical model	10	27 Nov	SIA + SIC
3.	FIO-ESM	FIO-ESM	Coupled dynamical model	1	15 Nov	SIA
4.	ECMWF	ecmwf	Coupled dynamical model	51	30 Nov	SIA + rSIA
5.	Lamont Sea Ice Group	Lamont	Statistical model	1	31 Oct	SIA + rSIA + SIC (monthly, interp. daily)
6.	NASA-GSFC	NASA-GSFC	Statistical model	1	30 Nov	SIA
7.	Modified_CanSIPS	Modified_CanSIPS	Coupled dynamical model	20	30 Nov	SIA + rSIA
8.	Met Office	MetOffice	Coupled dynamical model	42	25 Nov	SIA + rSIA + SIC
9.	CNRM	CNRM	Coupled dynamical model	51	30 Nov	SIA + rSIA + SIC
10.	UCLouvain	ucl	Ocean–Sea Ice dynamical model	10	1 Jul	SIA + rSIA + SIC
11.	Sandra Barreira	barreira	Statistical model	1	30 Nov	SIA + SIC

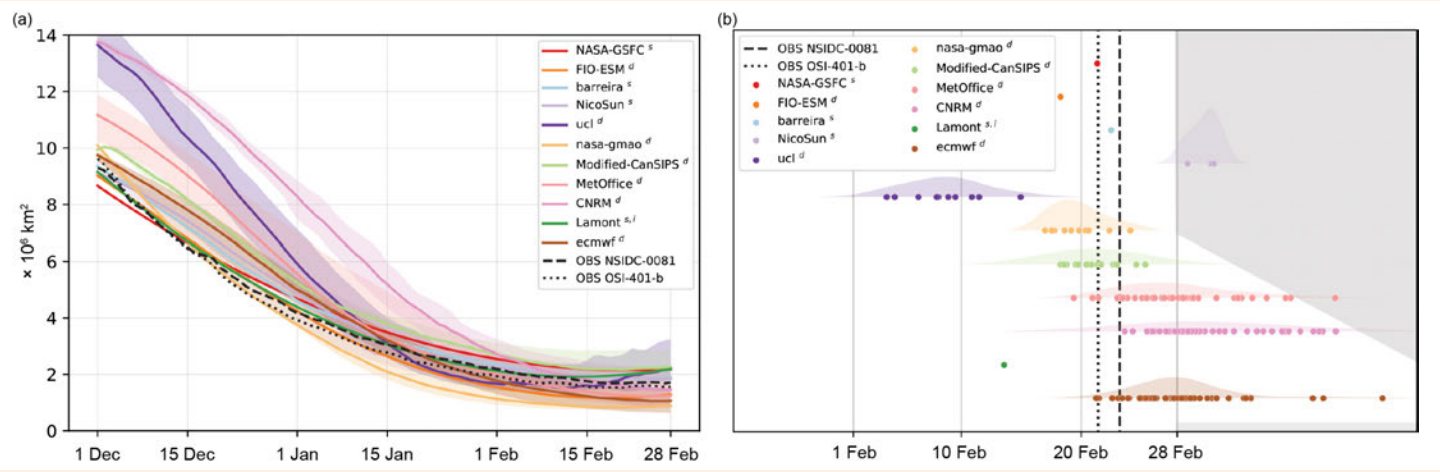

Fig. SB6.4. (a) Total (circumpolar) Antarctic SIA (× 10^6 km^2) of the 11 forecasts for each day of Dec–Feb 2019/20. The superscripts in the legend indicate whether the submission is based on a statistical or a dynamical approach. The black dashed lines are two observational references up to 21 Dec 2019. (b) Timing of the 2020 annual minimum Antarctic SIA from forecasts (colors) and two observational references (Maslanik and Stroeve 1999; Tonboe et al. 2017). To filter out the effects of synoptic variability, the minimum was determined from a quadratic fit of the Feb daily SIA time series. Superscripts in the legend indicate whether the submission is based on a statistical or a dynamical approach and, possibly, if monthly data has been interpolated to daily resolution.

SIA forecast for each day of December–February 2019/20. We understand that SIA may not be the most suitable geophysical diagnostic to assess model performance, but it gives a valuable first indication of how the forecasts behave. Figure SB6.4a also includes SIA from two observational sources, the NSIDC-0081 product (Near-Real-Time DMSP SSMIS Daily Polar Gridded Sea Ice Concentrations; Maslanik and Stroeve 1999) and the OSI-401-b product (Global Sea Ice Concentration; Tonboe et al. 2017) for comparison. (Two SIPN-South forecasts based on dynamical coupled models appear to be biased high at the time of initialization.)

Seven groups submitted spatial information of daily SIC for each day of December–February 2019/20. These groups provided several forecast members (from 1 to 42) to sample uncertainty associated with the (unpredictable) evolution of the climate system, so that each member of a given model can be seen as a possible realization of that model. Based on these forecasts, Fig. SB6.5 shows the modeled daily probability of sea ice presence on 15 February 2020, which can serve as useful information to ship operators when assessing potential areas of operation. Green pixels are those where the sea ice is unlikely to be present, while red ones are those where the sea ice is likely to be present.

The model ensembles are designed to sample weather variability, and results from Fig. SB6.5 indicate that weather can drive sea ice variability in key sectors like the Ross Sea, a region that proved very difficult to forecast during the previous two exercises. Whether those forecasts are correctly calibrated can be investigated once more retrospective forecasts are available, although this is beyond the scope of the SIPN-South project.

Figure SB6.4b illustrates the timing of the 2020 annual minimum Antarctic SIA from forecasts (colors) and two observational references. The minimum was correctly predicted by four forecasts when compared with the OSI-401-b observations and two forecasts when assessed against the NSIDC-0081 observations.

In summary, while we acknowledge that more hindcasts are necessary to ensure the robustness of the results, the analysis of three forecast exercises has already revealed several key outcomes:

- When viewed as an ensemble, the range of multi-model forecast of total February Antarctic SIA includes the actual observed state (Massonnet et al. 2018, 2019). However, errors can be large for individual submissions. Observational uncertainty alone cannot explain the forecast-observation mismatch (Maslanik and Stroeve 1999; Tonboe et al. 2017);
- The timing of minimum Antarctic SIA is not well predicted by the ensemble. The date of the minimum is in part driven by the seasonal change in insolation (which is predictable) but can be modulated by a few days by the passage of synoptic weather systems. Models, regardless of their nature, should capture weather uncertainty, but it appears that the ensemble spread is generally too narrow;
- In the first two SIPN-South experiments, the statistical contributions outperformed other contributions with respect to prediction of the timing of the annual minimum;
- At this stage of development, the SIPN-South data set is not yet mature enough for practical application to field experiment planning or maritime route forecasting in the Antarctic sea ice zone. Long records of retrospective forecasts are lacking in order to properly identify the origin of systematic forecast errors.

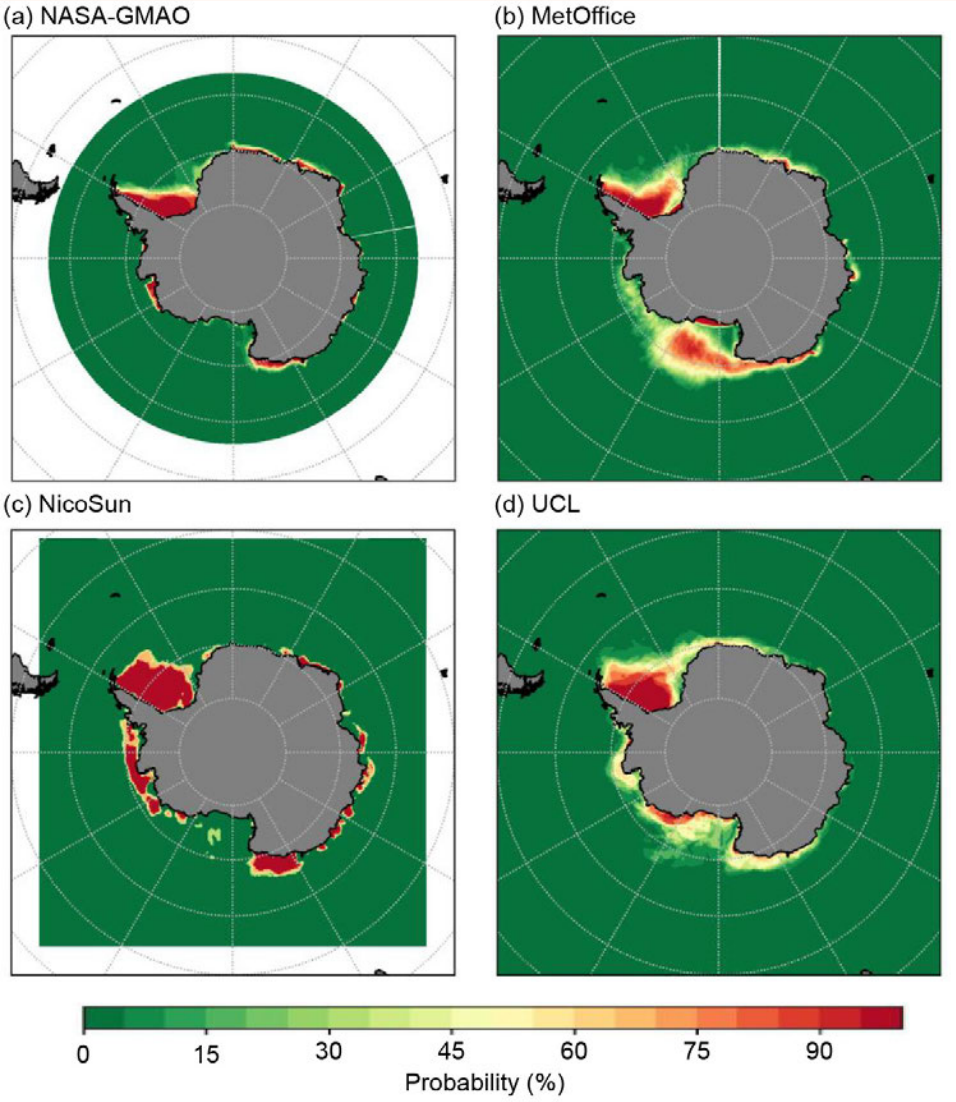

Fig. SB6.5. Probability of sea ice presence (%) for 15 Feb 2020, as forecast by the four groups that submitted daily SIC information. The probability of presence corresponds to the fraction of ensemble members that simulate SIC larger than 15% in a given grid cell for that day. A daily dynamic animation of that figure for 1–28 February is available at https://fmassonn.github.io/sipn-south.github.io/pics/2019-2020/probability.gif.

Acknowledgments

Ted Scambos was supported under NASA grant 17-MEASURES-0075, ITS_LIVE and NSF ANT 0944763, the Antarctic Glaciological Data Center.

Sharon Stammerjohn was supported under NSF PLR 1440435; she also thanks the Institute of Arctic and Alpine Research and the National Snow and Ice Data Center, both at the University of Colorado Boulder, for institutional and data support.

The work of Phil Reid and Rob Massom was supported by the Australian Government's Australian Antarctic Partnership Program, and contributes to AAS Project 4116. Phil Reid and Jan Lieser were also supported through the Australian Bureau of Meteorology, and Rob Massom by the Australian Antarctic Division.

Sandra Barreira was supported by the Argentine Hydrographic Service – Naval Meteorological Service.

Helen Amanda Fricker was supported by the NASA Cryospheric Sciences Program in support of the ICESat-2 mission under awards NNX15AC80G.

Alex Gardner was supported by funding from the NASA Cryosphere and MEaSUReS programs.

Povl Abrahamsen was supported by NERC grant NE/N018095/1.

Support for Linda Keller, David Mikolajczyk, and Matt Lazzara is courtesy of the National Science Foundation, Office of Polar Programs, Grants #1543305 and #1924730.

The marine mammal data were collected and made freely available by the International MEOP Consortium and the national programs that contribute to it (http://www.meop.net). We acknowledge in particular major contributions in the Southern Ocean in 2019 from IMOS (Integrated Marine Observing System, Australia) and from SO-MEMO (Observing System - Mammals as samplers of the Ocean Environment, France).

Seb Swart was supported by a Wallenberg Academy Fellowship (WAF 2015.0186) and by the Swedish Research Council (VR 2019-04400). Swart and Marcel du Plessis are supported by the South African National Research Foundation (SANAP - SNA14071475720). NCEP_Reanalysis 2 data provided by the NOAA/OAR/ESRL PSD, Boulder, Colorado, USA, from their website at https://www.esrl.noaa.gov/psd/

The authors of Sidebar 6.3 appreciate the contributions to all the forecast exercises, particularly those presented here from Nico Sun, NASA-GMAO (Richard Cullather, Anna Borovikov, Eric Hackert, Robin Kovach, Zhao Li, Jelena Marshak, Andrea Molod, Steven Pawson, Yury Vikhliaev, Bin Zhao), FIO-ESM (Fangli Qiao, Zhenya Song, Xunqiang Yin, Yajuan Song), NASA-GSFC (Alek Petty), Met Office (Ed Blockley, GloSea5 Seasonal Forecast team), Sandra Barreira and Alvaro Scardilli, as well as UC Louvain (Sylvain Marchi, François Massonnet).

APPENDIX: Acronym List

ABS	Amundsen and Bellingshausen Seas
ACC	Antarctic Circumpolar Current
AIS	Antarctic Ice Sheet
ClO	chlorine monoxide
CDW	Circumpolar Deep Water
DMSP	Defense Meteorological Satellite Program
DU	Dobson Units
EAIS	East Antarctic Ice Sheet
EESC	effective equivalent stratospheric chlorine
ENSO	El Niño–Southern Oscillation
ECMWF	European Centre for Medium-Range Weather Forecast
ISD	ice season duration
IMBIE	Ice-sheet Mass Balance Inter-comparison Experiment
IOD	Indian Ocean dipole
IPCC	Intergovernmental Panel on Climate Change
IMO	International Maritime Organization
MEOP	Marine Mammals Exploring the Oceans Pole to Pole
MBM	mass budget method
ME	melt extent
MI	melt index
MLS	Microwave Limb Sounder
NSIDC	National Snow and Ice Data Center
NH	Northern Hemisphere
ODS	ozone-depleting substances
PSCs	polar stratospheric clouds
SIA	sea ice area
SIC	sea ice concentration
SIE	sea ice extent
SIPN	Sea Ice Predication Network
SST	sea surface temperature
SAM	Southern Annual Mode
SH	Southern Hemisphere
SOCCOM	Southern Ocean Carbon and Climate Observations and Modeling
SSMIS	Special Sensor Microwave–Imager Sounder
SMB	surface mass balance

References

Abrahamsen, E. P., and Coauthors, 2019: Stabilization of dense Antarctic water supply to the Atlantic Ocean overturning circulation. *Nat. Climate Change*, **9**, 742–746, https://doi.org/10.1038/s41558-019-0561-2.

Agosta, C., and Coauthors, 2019: Estimation of the Antarctic surface mass balance using the regional climate model MAR (1979–2015) and identification of dominant processes. *Cryosphere*, **13**, 281–296, https://doi.org/10.5194/tc-13-281-2019.

Armstrong, R., K. Knowles, M. J. Brodzik, and M. A. Hardman, 1994: DMSP SSM/I-SSMIS pathfinder daily EASE-grid brightness temperatures, version 2. NASA NSIDC DAAC, accessed 12 February 2020, https://doi.org/10.5067/3EX2U1DV3434.

Bintanja, R., G. J. van Oldenborgh, S. S. Drijfhout, B. Wouters, and C. A. Katsman, 2013: Important role for ocean warming and increased ice-shelf melt in Antarctic sea-ice expansion. *Nat. Geosci.*, **6**, 376–379, https://doi.org/10.1038/ngeo1767.

Bourassa, M. A., and Coauthors, 2013: High-latitude ocean and sea ice surface fluxes: Challenges for climate research. *Bull. Amer. Meteor. Soc.*, **94**, 403–423, https://doi.org/10.1175/BAMS-D-11-00244.1.

Bushinsky, S. M., and Coauthors, 2019: Reassessing Southern Ocean air-sea CO2 flux estimates with the addition of biogeochemical float observations. *Global Biogeochem. Cycles*, **33**, 1370–1388, https://doi.org/10.1029/2019GB006176.

Castagno, P., V. Capozzi, G. R. DiTullio, P. Falco, G. Fusco, S. R. Rintoul, G. Spezie, and G. Budillon, 2019: Rebound of shelf water salinity in the Ross Sea. *Nat. Commun.*, **10**, 5441, https://doi.org/10.1038/s41467-019-13083-8.

Cavalieri, D. J., and Coauthors, 1996: Sea ice concentrations from Nimbus-7 SMMR and DMSP SSM/I-SSMIS passive microwave data, version 1. NASA NSIDC DAAC, accessed 12 February 2020, https://doi.org/10.5067/8GQ8LZQVL0VL.

Chen, J. L., C. R. Wilson, D. N. D. Blankenship, and B. D. Tapley, 2009: Accelerated Antarctic ice loss from satellite gravity measurements. *Nat. Geosci.*, **2**, 859–862, https://doi.org/10.1038/ngeo694.

Comiso, J. C., R. A. Gersten, L. V. Stock, J. Turner, G. J. Perez, and K. Cho, 2016: Positive trend in the Antarctic sea ice cover and associated changes in surface temperature. *J. Climate*, 30, 2251–2267, https://doi.org/10.1175/JCLI-D-16-0408.1.

COMNAP, 2015: COMNAP Sea Ice Challenges Workshop. Workshop Rep., Council of Managers of National Antarctic Programs, 71 pp., www.comnap.aq/documents/COMNAP_Sea_Ice_Challenges_BKLT_Web_Final_Dec2015.pdf.

Copernicus Climate Change Service 2017: ERA5: Fifth generation of ECMWF atmospheric reanalyses of the global climate. Copernicus Climate Change Service Climate Data Store, accessed 4 May 2018, https://cds.climate.copernicus.eu/cdsapp#!/home/.

Depoorter, M. A., J. L. Bamber, J. A. Griggs, J. T. M. Lenaerts, S. R. M. Ligtenberg, M. R. van den Broeke, and G. Moholdt, 2013: Calving fluxes and basal melt rates of Antarctic ice shelves. *Nature*, **502**, 89–92, https://doi.org/10.1038/nature12567.

Desbruyères, D. G., S. G. Purkey, E. L. McDonagh, G. C. Johnson, and B. A. King, 2016: Deep and abyssal ocean warming from 35 years of repeat hydrography. *Geophys. Res. Lett.*, **43**, 10356–10365, https://doi.org/10.1002/2016GL070413.

Fay, A. R., G. A. McKinley, and N. S. Lovenduski, 2014: Southern Ocean carbon trends: Sensitivity to methods. *Geophys. Res. Lett.*, **41**, 6833–6840, https://doi.org/10.1002/2014GL061324.

Gardner, A. S., G. Moholdt, T. Scambos, M. Fahnstock, S. Ligtenberg, M. Van Den Broeke, and J. Nilsson, 2018: Increased West Antarctic and unchanged East Antarctic ice discharge over the last 7 years. *Cryosphere*, **12**, 521–547, https://doi.org/10.5194/tc-12-521-2018.

Gelaro, R., and Coauthors, 2017: The Modern-Era Retrospective Analysis for Research and Applications, version 2 (MERRA-2). *J. Climate*, **30**, 5419–5454, https://doi.org/10.1175/JCLI-D-16-0758.1.

Gordon, A. L., B. A. Huber, and E. P. Abrahamsen, 2020: Interannual variability of the outflow of Weddell Sea Bottom Water. Geophys. Res. Lett., 47, e2020GL087014, https://doi.org/10.1029/2020GL087014.

Gossart, A., S. Helsen, J. T. M. Lenaerts, S. Vanden Broucke, N. P. M. van Lipzig, and N. Souverijns, 2019: An evaluation of surface climatology in state-of-the-art reanalyses over the Antarctic ice sheet. *J. Climate*, **32**, 6899–6915, https://doi.org/10.1175/JCLI-D-19-0030.1.

Gray, A. R., and Coauthors, 2018: Autonomous biogeochemical floats detect significant carbon dioxide outgassing in the high-latitude Southern Ocean. *Geophys. Res. Lett.*, **45**, 9049–9057, https://doi.org/10.1029/2018GL078013.

Gregor, L., S. Kok, and P. M. S. Monteiro, 2018: Interannual drivers of the seasonal cycle of CO2 in the Southern Ocean. *Biogeosciences*, **15**, 2361–2378, https://doi.org/10.5194/bg-15-2361-2018.

——, A. D. Lebehot, , S. Kok, and P. M. S. Monteiro, 2019: A comparative assessment of the uncertainties of global surface ocean CO_2 estimates using a machine-learning ensemble (CSIR-ML6 version 2019a) — Have we hit the wall? *Geosci. Model Dev.*, **12**, 5113–5136, https://doi.org/10.5194/gmd-12-5113-2019.

Gudmundsson, G. H., F. S. Paolo, S. Adusumilli, and H. A. Fricker, 2019: Instantaneous Antarctic ice sheet mass loss driven by thinning ice shelves. *Geophys. Res. Lett.*, **46**, 13903–13909, https://doi.org/10.1029/2019GL085027.

Hamilton, L. C., and J. Stroeve, 2016: 400 predictions: The search sea ice outlook 2008–2015. *Polar Geogr.*, **39**, 274–287, https://doi.org/10.1080/1088937X.2016.1234518.

Haumann, F. A., N. Gruber, and M. Münnich, 2020: Sea-ice induced Southern Ocean subsurface warming and surface cooling in a warming climate. *AGU Adv.*, **1**, e2019AV000132, https://doi.org/10.1029/2019AV000132.

Holland, P. R., T. J. Bracegirdle, P. Dutrieux, A. Jenkins, and E. J. Steig, 2019: West Antarctic ice loss influenced by internal climate variability and anthropogenic forcing. *Nat. Geosci.*, **12**, 718–724, https://doi.org/10.1038/s41561-019-0420-9.

IMBIE Team, 2018: Mass balance of the Antarctic ice sheet from 1992 to 2017. *Nature*, **558**, 219–222, https://doi.org/10.1038/s41586-018-0179-y.

IMO, 2017: International code for ships operating in polar waters (polar code). International Maritime Organization, www.imo.org/en/MediaCentre/HotTopics/polar/Pages/default.aspx.

Jacobs, S. S., and C. F. Giulivi, 2010: Large multidecadal salinity trends near the Pacific–Antarctic continental margin. *J. Climate*, **23**, 4508–4524, https://doi.org/10.1175/2010JCLI3284.1.

Johnson, G. C., 2008: Quantifying Antarctic bottom water and North Atlantic deep water volumes. *J. Geophys. Res.*, **113**, C05027, https://doi.org/10.1029/2007JC004477.

Johnson, K. S., and Coauthors, 2017: Biogeochemical sensor performance in the SOCCOM profiling float array. *J. Geophys. Res. Oceans*, **122**, 6416–6436, https://doi.org/10.1002/2017JC012838.

Josey, S. A., S. Gulev, and L. Yu, 2013: Exchanges through the ocean surface. Ocean Circulation and Climate: A 21st Century Perspective, G. Siedler et al., Eds., Academic Press, 115–140, https://doi.org/10.1016/b978-0-12-391851-2.00005-2.

Jullion, L., A. C. Naveira Garabato, M. P. Meredith, P. R. Holland, P. Courtois, and B. A. King, 2013: Decadal freshening of the Antarctic bottom water exported from the Weddell Sea. *J. Climate*, **26**, 8111–8125, https://doi.org/10.1175/JCLI-D-12-00765.1.

Jung, T., and Coauthors, 2016: Advancing polar prediction capabilities on daily to seasonal time scales. *Bull. Amer. Meteor. Soc.*, **97**, 1631–1647, https://doi.org/10.1175/BAMS-D-14-00246.1.

Kanamitsu, M., W. Ebisuzaki, J. Woollen, S. Yang, J. J. Hnilo, M. Fiorino, and G. L. Potter, 2002: NCEP–DOE AMIP-II Reanalysis (R-2). *Bull. Amer. Meteor. Soc.*, **83**, 1631–1644, https://doi.org/10.1175/BAMS-83-11-1631.

Keppler, L., and P. Landschützer, 2019: Regional wind variability modulates the Southern Ocean carbon sink. *Sci. Rep.*, **9**, 7384, https://doi.org/10.1038/s41598-019-43826-y.

Landschützer, P., N. Gruber, and D. C. E. Bakker, 2016: Decadal variations and trends of the global ocean carbon sink. *Global Biogeochem. Cycles*, **30**, 1396–1417, https://doi.org/10.1002/2015GB005359.

Langematz, U., and Coauthors 2018: Polar stratospheric ozone: Past, present, and future. Scientific assessment of ozone depletion: 2018, Global Ozone Research and Monitoring Project Rep. 58, World Meteorological Organization, 4.1–4.63, https://ozone.unep.org/sites/default/files/2019-05/SAP-2018-Assessment-report.pdf.

Lazzara, M. A., K. C. Jezek, T. A. Scambos, D. R. MacAyeal, and C. J. Van der Veen, 1999: On the recent calving of icebergs from the Ross Ice Shelf. *Polar Geogr.*, **23**, 201–212, https://doi.org/10.1080/10889379909377676.

Lenaerts, J. T. M., and M. R. Van Den Broeke, 2012: Modeling drifting snow in Antarctica with a regional climate model: 2. Results. *J. Geophys. Res.*, **117**, D05109, https://doi.org/10.1029/2010JD015419.

——, E. van Meijgaard, M. R. van den Broeke, S. R. M. Ligtenberg, M. Horwath, and E. Isaksson, 2013: Recent snowfall anomalies in Dronning Maud Land, East Antarctica, in a historical and future climate perspective. *Geophys. Res. Lett.*, **40**, 2684–2688, https://doi.org/10.1002/grl.50559.

Lim, E.-P., H. H. Hendon, and D. W. J. Thompson, 2018: Seasonal evolution of stratosphere-troposphere coupling in the Southern Hemisphere and implications for the predictability of surface climate. *J. Geophys. Res. Atmos.*, **123**, 12 002–12 016, https://doi.org/10.1029/2018JD029321.

——, ——, G. Boschat, D. Hudson, D. W. Thompson, A. J. Dowdy, and J. M. Arblaster, 2019: Australian hot and dry extremes induced by weakenings of the stratospheric polar vortex. *Nat. Geosci.*, **12**, 896–901, https://doi.org/10.1038/s41561-019-0456-x.

Liu, H., L. Wang, and K. Jezek, 2005: Wavelet- transform based edge detection approach to derivation of snowmelt onset, end and duration from satellite passive microwave measurements. *Int. J. Remote Sens.*, **26**, 4639–4660, https://doi.org/10.1080/01431160500213342.

—, —, and —, 2006: Spatio-temporal variations of snow melt zones in Antarctic Ice Sheet derived from satellite SMMR and SSM/I data (1978–2004). *J. Geophys. Res.*, **111**, F01003, https://doi.org/10.1029/2005JF000318.

Liu, J., X. Tingyin, and L. Chen, 2011: Intercomparisons of air–sea heat fluxes over the Southern Ocean. *J. Climate*, **24**, 1198–1211, https://doi.org/10.1175/2010jcli3699.1.

Manney, G. L., and Coauthors, 2011: Unprecedented Arctic ozone loss in 2011. *Nature*, **478**, 469–475, https://doi.org/10.1038/nature10556.

Marchi, S., T. Fichefet, H. Goosse, V. Zunz, S. Tietsche, J. J. Day, and, E. Hawkins, 2018: Reemergence of Antarctic sea ice predictability and its link to deep ocean mixing in global climate models. *Climate Dyn.*, **52**, 2775–2797, https://doi.org/10.1007/S00382-018-4292-2.

Marshall, G. J., 2003: Trends in the southern annular mode from observations and reanalyses. *J. Climate*, **16**, 4134–4143, https://doi.org/10.1175/1520-0442(2003)016%3C4134:TITSAM%3E2.0.CO;2.

Maslanik, J., and J. Stroeve, 1999: Near-Real-Time DMSP SSM/I-SSMIS daily polar gridded sea ice concentrations, version 1. Updated daily, NASA NSIDC DAAC, accessed 12 February 2020, https://doi.org/10.5067/U8C09DWVX9LM.

Massom, R. A., and S. E. Stammerjohn, 2010: Antarctic sea ice change and variability - Physical and ecological implications. *Polar Sci.*, **4**, 149–186, https://doi.org/10.1016/j.polar.2010.05.001.

——, T. A. Scambos, L. G. Bennetts, P. Reid, V. A. Squire, and S. E. Stammerjohn, 2018: Antarctic ice shelf disintegration triggered by sea ice loss and ocean swell. *Nature*, **558**, 383–389, https://doi.org/10.1038/s41586-018-0212-1.

Massonnet, F., P. Reid, J. L. Lieser, C. M. Bitz, J. Fyfe, and W. Hobbs, 2018: Assessment of February 2018 sea-ice forecasts for the Southern Ocean. Antarctic Climate and Ecosystems Cooperative Research Centre Tech. Rep., University of Tasmania, 12 pp., https://doi.org/10.4226/77/5b343caab0498.

—, —,—, —, —, and —, 2019: Assessment of summer 2018-2019 sea-ice forecasts for the Southern Ocean. Antarctic Climate and Ecosystems Cooperative Research Centre Tech. Rep., University of Tasmania, 13 pp., https://doi.org/10.25959/100.00029984.

McKee, D. C., X. Yuan, A. L. Gordon, B. A. Huber, and Z. Dong, 2011: Climate impact on interannual variability of Weddell Sea bottom water. *J. Geophys. Res.*, **116**, C05020, https://doi.org/10.1029/2010JC006484.

Medley, B., and E. R. Thomas, 2019: Increased snowfall over the Antarctic Ice Sheet mitigated twentieth-century sea-level rise. *Nat. Climate Change*, **9**, 34–39, https://doi.org/10.1038/s41558-018-0356-x.

Meehl, G. A., and Coauthors, 2019: Sustained ocean changes contributed to sudden Antarctic sea ice retreat in late 2016. *Nat. Commun.*, **10**, 14, https://doi.org/10.1038/s41467-018-07865-9.

Menezes, V. V., A. M. Macdonald, and C. Schatzman, 2017: Accelerated freshening of Antarctic bottom water over the last decade in the Southern Indian ocean. *Sci. Adv.*, **3**, e1601426, https://doi.org/10.1126/sciadv.1601426.

Mottram, R., and Coauthors, 2020: What is the surface mass balance of Antarctica? An intercomparison of regional climate model estimates. *Cryosphere Discuss.*, https://doi.org/10.5194/tc-2019-333.

Narayanan, A., S. T. Gille, M. R. Mazloff, and K. Murali, 2019: Water mass characteristics of the Antarctic margins and the production and seasonality of Dense Shelf Water. *J. Geophys. Res. Oceans*, **124**, 9277–9294, https://doi.org/10.1029/2018JC014907.

Palm, S. P., V. Kayetha, and Y. Yang, 2018: Toward a satellite-derived climatology of blowing snow over Antarctica. *J. Geophys. Res. Atmos.*, **123**, 10 301–10 313, https://doi.org/10.1029/2018JD028632.

Paolo, F. S., H. A. Fricker, and L. Padman, 2015: Volume loss from Antarctic ice shelves is accelerating. *Science*, **348**, 327–331, https://doi.org/10.1126/science.aaa0940.

——, L. Padman, H. A. Fricker, S. Adusumilli, S. Howard, and M. R. Siegfried, 2018: Response of Pacific-sector Antarctic ice shelves to the El Niño/Southern Oscillation. *Nat. Geosci.*, **11**, 121–126, https://doi.org/10.1038/s41561-017-0033-0.

Pitts, M. C., L. R. Poole, and R. Gonzalez, 2018: Polar stratospheric cloud climatology based on CALIPSO spaceborne lidar measurements from 2006 to 2017. *Atmos. Chem. Phys.*, **18**, 10 881–10 913, https://doi.org/10.5194/acp-18-10881-2018.

Pope, J. O., P. R. Holland, A. Orr, G. J. Marshall, and T. Phillips, 2017: The impacts of El Niño on the observed sea ice budget of West Antarctica. *Geophys. Res. Lett.*, **44**, 6200–6208, https://doi.org/10.1002/2017GL073414.

Pritchard, H. D., R. J. Arthern, D. G. Vaughan, and L. A. Edwards, 2009: Extensive dynamic thinning on the margins of the Greenland and Antarctic ice sheets. *Nature*, **461**, 971–975, https://doi.org/10.1038/NATURE08471.

——, S. R. M. Ligtenberg, H. A. Fricker, D. G. Vaughan, M. R. van den Broeke, and L. Padman, 2012: Antarctic ice-sheet loss driven by basal melting of ice shelves. *Nature*, **484**, 502–505, https://doi.org/10.1038/nature10968.

Purkey, S. G., and G. C. Johnson, 2012: Global contraction of Antarctic bottom water between the 1980s and 2000s. *J. Climate*, **25**, 5830–5844, https://doi.org/10.1175/JCLI-D-11-00612.1.

——, and ——, 2013: Antarctic bottom water warming and freshening: Contributions to sea level rise, ocean freshwater budgets, and global heat gain. *J. Climate*, **26**, 6105–6122, https://doi.org/10.1175/JCLI-D-12-00834.1.

——, and Coauthors, 2019: Unabated bottom water warming and freshening in The south Pacific Ocean. *J. Geophys. Res. Oceans*, **124**, 1778–1794, https://doi.org/10.1029/2018JC014775.

Reid, P. A., and R. A. Massom, 2015: Successive Antarctic sea ice extent records during 2012, 2013 and 2014 [in "State of the Climate in 2014"]. *Bull. Amer. Meteor. Soc.*, **96** (7), S163–S164, https://doi.org/10.1175/2015BAMSStateoftheClimate.1.

——, S. Stammerjohn, R. A. Massom, S. Barreira, T. Scambos, and J. Lieser, 2018: Sea ice extent, concentration and seasonality [in "State of the Climate in 2017"]. *Bull. Amer. Meteor. Soc.*, **99** (8), S183–S185, https://doi.org/10.1175/2018BAMSStateoftheClimate.1.

——, ——, ——, ——, ——, and ——, 2019: Sea ice extent, concentration and seasonality [in "State of the Climate in 2018"]. *Bull. Amer. Meteor. Soc.*, **100** (9), S178–S181, https://doi.org/10.1175/2019BAMSStateoftheClimate.1.

Reynolds, R. W., N. A. Rayner, T. M. Smith, D. C. Stokes, and W. Wang, 2002: An improved in situ and satellite SST analysis for climate. *J. Climate*, **15**, 1609–1625, https://doi.org/10.1175/1520-0442(2002)015<1609:AIISAS>2.0.CO;2.

Rignot, E., J. L. Bamber, M. R. Van Den Broeke, C. Davis, Y. Li, W. J. Van De Berg, and E. Van Meijgaard, 2008: Recent Antarctic ice mass loss from radar interferometry and regional climate modelling. *Nat. Geosci.*, **1**(2), 106–110, https://doi.org/10.1038/ngeo102

——, S. Jacobs, J. Mouginot, and B. Scheuchl, 2013: Ice-shelf melting around Antarctica. *Science*, **341**, 266–270, https://doi.org/10.1126/science.1235798.

——, J. Mouginot, B. Scheuchl, M. van den Broeke, M. J. van Wessem, and M. Morlighem, 2019: Four decades of Antarctic ice sheet mass balance from 1979–2017. *Proc. Natl. Acad. Sci. USA*, **116**, 1095–1103, https://doi.org/10.1073/pnas.1812883116.

Roquet, F., and Coauthors, 2014: A Southern Indian Ocean database of hydrographic profiles obtained with instrumented elephant seals. *Nature*, **1**, 140028, https://doi.org/10.1038/sdata.2014.28.

Shepherd, A., D. J. Wingham, J. A. D. Mansley, and H. F. J. Corr, 2001: Inland thinning of pine Island glacier, West Antarctica. *Science*, **291**, 862–864, https://doi.org/10.1126/SCIENCE.291.5505.862.

——, and Coauthors, 2012: A reconciled estimate of ice-sheet mass balance. *Science*, **338**, 1183–1189, https://doi.org/10.1126/science.1228102.

——, and Coauthors, 2019: Trends in Antarctic ice sheet elevation and mass. *Geophys. Res. Lett.*, **46**, 8174–8183, https://doi.org/10.1029/2019GL082182.

Smith, B., and Coauthors, 2020: Pervasive ice sheet mass loss reflects competing ocean and atmosphere processes. *Science*, **368**, 1239–1242, https://doi.org/10.1126/SCIENCE.AAZ5845.

Smith, T. M., R. W. Reynolds, T. C. Peterson, and J. Lawrimore, 2008: Improvements to NOAA's historical merged land–ocean surface temperature analysis (1880–2006). *J. Climate*, **21**, 2283–2296, https://doi.org/10.1175/2007JCLI2100.1.

St-Laurent, P., P. L. Yager, R. M. Sherrell, S. E. Stammerjohn, and M. S. Dinniman, 2017: Pathways and supply of dissolved iron in the Amundsen Sea (Antarctica). *J. Geophys. Res. Oceans*, **122**, 7135–7162, https://doi.org/10.1002/2017JC013162.

Stammerjohn, S. E., D. G. Martinson, R. C. Smith, X. Yuan, and D. Rind, 2008: Trends in Antarctic annual sea ice retreat and advance and their relation to El Niño–Southern Oscillation and southern annular mode variability. *J. Geophys. Res.*, **113**, C03S90, https://doi.org/10.1029/2007JC004269.

——, and Coauthors, 2015: Seasonal sea ice changes in the Amundsen Sea, Antarctica, over the period of 1979–2014. *Elementa*, **3**, 00005, https://doi.org/10.12952/JOURNAL.ELEMENTA.000055.

Steig, E. J., Q. Ding, D. S. Battisti, and A. Jenkins, 2012: Tropical forcing of circumpolar deep water inflow and outlet glacier thinning in the Amundsen Sea embayment, west Antarctica. *Ann. Glaciol.*, **53**, 19–28, https://doi.org/10.3189/2012AoG60A110.

Swart, S., S. Speich, I. J. Ansorge, and J. R. E. Lutjeharms, 2010: An altimetry-based gravest empirical mode south of Africa: 1. Development and validation. *J. Geophys. Res.*, **115**, C03002, https://doi.org/10.1029/2009JC005299.

——, and Coauthors, 2019: Constraining Southern Ocean air-sea-ice fluxes through enhanced observations. *Front. Mar. Sci.*, **6**, 421, https://doi.org/10.3389/fmars.2019.00421.

Tedesco, M., 2009a: Assessment and development of snowmelt retrieval algorithms over Antarctica from K-band spaceborne brightness temperature (1979-2008). *Remote Sens. Environ.*, **113**, 979–997, https://doi.org/10.1016/j.rse.2009.01.009.

——, 2009b: An updated Antarctic melt record through 2009 and its linkages to high-latitude and tropical climate variability. *Geophys. Res. Lett.*, **36**, L18502, https://doi.org/10.1029/2009GL039186.

Thoma, M., A. Jenkins, D. Holland, and S. Jacobs, 2008: Modelling circumpolar deep water intrusions on the Amundsen Sea continental shelf, Antarctica. *Geophys. Res. Lett.*, **35**, L18602, https://doi.org/10.1029/2008GL034939.

Thomas, D. N., Ed., 2017: Sea Ice. 3rd ed. Wiley-Blackwell, 645 pp.

Thomas, R. H., 1979: The dynamics of marine ice sheets. *J. Glaciol.*, **24**, 167–177, https://doi.org/10.3189/S0022143000014726.

Timmermann, R., and H. H. Hellmer, 2013: Southern Ocean warming and increased ice shelf basal melting in the twenty-first and twenty-second centuries based on coupled ice-ocean finite-element modelling. *Ocean Dyn.*, **63**, 1011–1026, https://doi.org/10.1007/s10236-013-0642-0.

Tonboe, R., J. Lavelle, R. H. Pfeiffer, and E. Howe, 2017: Product user manual for OSI SAF Global Sea Ice Concentration (Product OSI-401-b), version 1.6. OSI SAF, 25 pp., http://osisaf.met.no/docs/osisaf_cdop3_ss2_pum_ice-conc_v1p6.pdf.

Treasure, A. M., and Coauthors, 2017: Marine mammals exploring the oceans pole to pole: A review of the MEOP consortium. *Oceanography*, **30**, 132–138, https://doi.org/10.5670/oceanog.2017.234.

Turner, J., and Coauthors, 2004: The SCAR READER project: Toward a high-quality database of mean Antarctic meteorological observations. *J. Climate*, **17**, 2890–2898, https://doi.org/10.1175/1520-0442(2004)017<2890:TSRPTA>2.0.CO;2.

——, and Coauthors, 2016: Absence of 21st century warming on Antarctic Peninsula consistent with natural variability. *Nature*, **535**, 411–415, https://doi.org/10.1038/nature18645.

Velicogna, I., 2009: Increasing rates of ice mass loss from the Greenland and Antarctic ice sheets revealed by GRACE. *Geophys. Res. Lett.*, **36**, L19503, https://doi.org/10.1029/2009GL040222.

——, T. C. Sutterley, and M. R. van den Broeke, 2014: Regional acceleration in ice mass loss from Greenland and Antarctica using GRACE time-variable gravity data. *Geophys. Res. Lett.*, **41**, 8130–8137, https://doi.org/10.1002/2014GL061052.

—, and Coauthors, 2020: Continuity of ice sheet mass loss in Greenland and Antarctica from the GRACE and GRACE follow-on missions. *Geophys. Res. Lett.*, **47**, e2020GL087291, https://doi.org/10.1029/2020GL087291.

Wang, Y., and Coauthors, 2016: A comparison of Antarctic Ice Sheet surface mass balance from atmospheric climate models and in situ observations. *J. Climate*, **29**, 5317–5337, https://doi.org/10.1175/JCLI-D-15-0642.1.

Williams, N. L., and Coauthors, 2017: Calculating surface ocean pCO2 from biogeochemical Argo floats equipped with pH: An uncertainty analysis. *Global Biogeochem. Cycles*, **31**, 591–604, https://doi.org/10.1002/2016GB005541.

Wingham, D. J., A. J. Ridout, R. Scharroo, R. J. Arthern, and C. K. Shum, 1998: Antarctic elevation change from 1992 to 1996. *Science*, **282**, 456–458, https://doi.org/10.1126/science.282.5388.456.

Yuan, X., M. R. Kaplan, and M. A. Cane, 2018: The interconnected global climate system-a review of tropical-polar teleconnections. *J. Climate*, **31**, 5765–5792, https://doi.org/10.1175/JCLI-D-16-0637.1.

Zwally, H. J., and S. Fiegles, 1994: Extent and duration of Antarctic surface melting. *J. Glaciol.*, **40**, 463–475, https://doi.org/10.3189/S0022143000012338.